Improvement of the high-accuracy $^{17}O(p,\alpha)^{14}N$ reaction-rate measurement via the Trojan Horse method for application to ^{17}O nucleosynthesis

M. L. Sergi,* C. Spitaleri, M. La Cognata, L. Lamia, R. G. Pizzone, and G. G. Rapisarda
INFN, Laboratori Nazionali del Sud, Catania, Italy
and Dipartimento di Fisica e Astronomia, Universitá degli studi di Catania, Catania, Italy

X. D. Tang, B. Bucher, M. Couder, P. Davies, R. deBoer, X. Fang, L. Lamm,† C. Ma, M. Notani, S. O'Brien, D. Roberson, W. Tan, and M. Wiescher
Department of Physics, Joint Institute for Nuclear Astrophysics, University of Notre Dame, Notre Dame 46556, Indiana, USA

B. Irgaziev
GIK Institute of Engineering Sciences and Technology, Topi, Districti Swabi, Khyber Pakhtunkhwa, Pakistan

A. Mukhamedzhanov
Cyclotron Institute, Texas A&M University, College Station, Texas 77843, USA

J. Mrazek and V. Kroha
Nuclear Physics Institute of ASCR, Rez, Czech Republi

The $^{17}O(p,\alpha)^{14}N$ and $^{17}O(p,\gamma)^{18}F$ reactions are of paramount importance for the nucleosynthesis in a number of stellar sites, including red giants (RGs), asymptotic giant branch (AGB) stars, massive stars, and classical novae. In particular, they govern the destruction of ^{17}O and the formation of the short-lived radioisotope ^{18}F, which is of special interest for γ-ray astronomy. At temperatures typical of the above-mentioned astrophysical scenario, $T = 0.01$–0.1 GK for RG, AGB, and massive stars and $T = 0.1$–0.4 GK for a classical nova explosion, the $^{17}O(p,\alpha)^{14}N$ reaction cross section is dominated by two resonances: one at about $E_R^{cm} = 65$ keV above the ^{18}F proton threshold energy, corresponding to the $E_X = 5.673$ MeV level in ^{18}F, and another one at $E_R^{cm} = 183$ keV ($E_X = 5.786$ MeV). We report on the indirect study of the $^{17}O(p,\alpha)^{14}N$ reaction via the Trojan Horse method by applying the approach recently developed for extracting the strength of narrow resonance at ultralow energies. The mean value of the strengths obtained in the two measurements was calculated and compared with the direct data available in literature. This value was used as input parameter for reaction-rate determination and its comparison with the result of the direct measurement is also discussed in the light of the electron screening effect.

I. INTRODUCTION

A. Astrophysical background

γ-ray lines from cosmic sources provide unique isotopic information, because they originate from energy-level transitions in the atomic nucleus. The role of novae as potential γ-ray emitters was mentioned long ago [1–3]. When the white dwarf accretes hydrogen-rich material from a less-evolved companion, some mixing at the base of the growing envelope enriches its C and O content [1]. When enough matter is accreted, a thermonuclear runaway is triggered through the hot CNO cycle, mixing radioactive ^{13}N, ^{14}O, and ^{15}O nuclei through the heated envelope. The subsequent β^+-decays and e^+-e^- annihilations supply the main power for accelerating about $10^{-4}M_\odot$ of the envelope to escape velocities equal to 1–2×10^3 km s^{-1}. Positron annihilation and nuclear deexcitation following the decays of these radioactive isotopes lead to γ-ray line fluxes. Their measurement would shed light into the physical processes occurring in the early phases of the explosion, although their detection is currently difficult to be performed owing to the still present observational difficulties, as discussed in Ref. [4].

The short-lived ^{13}N and the synthesized ^{18}F isotopes are the main contributors of positrons in nova envelopes. When ^{13}N decays, the nova envelope is still opaque; therefore, ^{18}F plays the most important role. Because of its longer lifetime, its decay occurs when the envelope begins to be transparent enough for γ rays to be emitted into space [5]. The main nuclear path leading to ^{18}F synthesis in novae belongs to the hot CNO cycles (see Fig. 1). Because in both carbon-oxygen and oxygen-neon novae the initial abundance of ^{16}O is large, ^{16}O is the main seed for ^{18}F formation through two possible chains of reactions:

$$^{16}O(p,\gamma)^{17}F(p,\gamma)^{18}Ne(\beta^+)^{18}F \quad (1)$$

and

$$^{16}O(p,\gamma\ )^{17}F(\beta^+)^{17}O(p,\gamma\ )^{18}F. \quad (2)$$

The ^{18}F destruction can occur either through β decay or through proton capture, by means of the $^{18}F(p,\gamma)^{19}Ne$ and the

*sergi@lns.infn.it
†Deceased

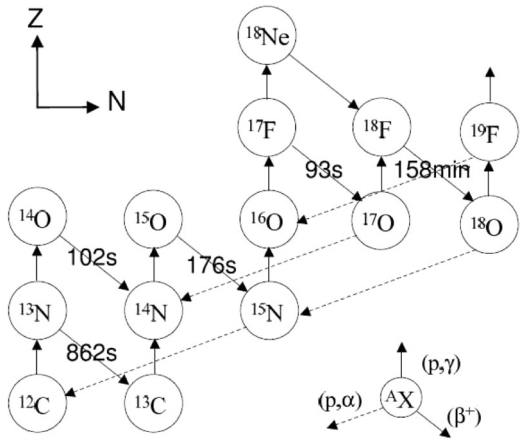

FIG. 1. Scheme of the carbon-nitrogen-oxygen (hot CNO) cycle of hydrogen burning which operates in nova explosions. The lifetimes of the unstable nuclei are displayed.

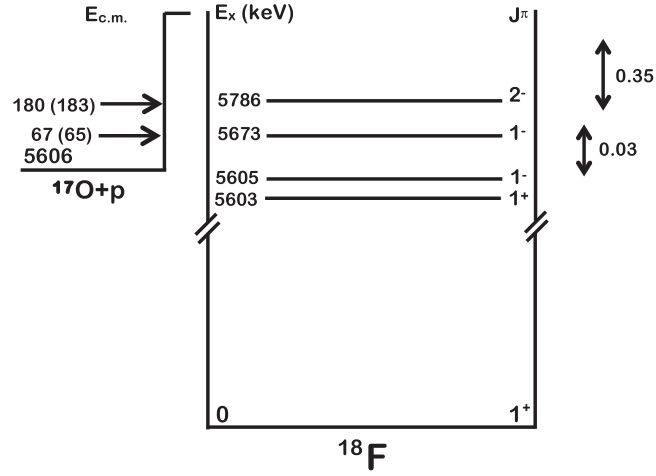

FIG. 2. Diagram of the ^{18}F levels intervening in the ^{17}O$(p,\alpha)\,^{14}$N up to energies of about 200 keV. The excitation energies and the J^π assignments are from Ref. [13]. The energy of the ^{17}O-p system in the center-of-mass reference system, $E_{\rm c.m.}$, of the observed resonances are indicated, as reported in Ref. [13]. The values in the parentheses are those measured in the recent works of Refs. [11,14]. The vertical arrows fix the Gamow windows for nova explosions ($T_9 = 0.35$) and AGB stars ($T_9 = 0.03$).

^{18}F$(p,\alpha)\,^{15}$O reactions [5]. With respect to the ^{18}F production, the ^{17}O$(p,\alpha)\,^{14}$N and ^{17}O$(p,\gamma)\,^{18}$F competing reactions are considered to be sources of major uncertainties [5,6]. The latter leads to the formation of ^{18}F from ^{16}O seed nuclei through the chain (2) while the former diverts the flow reducing both ^{18}F and ^{17}O yields.

Beyond the role played in novae nucleosynthesis, ^{17}O$(p,\alpha)\,^{14}$N is important for the interpretation of isotopic CNO abundances in meteoritic inclusions. These are important sources for determining the conditions in the atmosphere of red giant branch (RGB) and asymptotic giant branch (AGB) stars. In particular, the interpretation of the ^{17}O / ^{16}O versus ^{18}O / ^{16}O isotopic ratios in oxide grains could shed light in both AGB nucleosynthesis and possibly extra mixing phenomena not yet well understood (see Refs. [7–9]). Surface material can, in fact, be transported from the external layers down to hotter regions in which the nuclear ^{17}O burning could be activated at typical temperatures of $0.01 < T_9 < 0.1$ ($T_9 = T/10^9$ K) [10]. This requires higher accuracy measurements of the ^{17}O$(p,\alpha)\,^{14}$N cross section at the corresponding energies.

Thus, for all the reasons given above, the ^{17}O$(p,\alpha)\,^{14}$N reaction rate needs to be investigated at temperatures $T_9 =$ 0.01–0.1 for red giant, AGB, and massive stars and at $T_9 =$ 0.1–0.4 for classical nova explosions.

The ^{17}O$(p,\alpha)\,^{14}$N reaction cross section is expected to be dominated at stellar energies by a resonance at $E_{\rm c.m.} = 65$ keV, corresponding to the $E_X(J^\pi) = 5.673$ MeV (1^-) level in ^{18}F. A subthreshold level at $E_X(J^\pi) = 5.605$ MeV (1^-) could also play a significant role in the reaction rate both through its high-energy tail and because of possible interference effects with the 5.673-MeV level. Other states that could be involved in the stellar reaction rates are the $E_X(J^\pi) = 5.603$ MeV (1^+) level only bound by 3 keV against proton decay and the $E_X(J^\pi) = 5.786$ MeV (2^-) level for high-temperature processes, corresponding to the $E_{\rm c.m.} = 183$ keV resonance in the ^{17}O$(p,\alpha)\,^{14}$N reaction [11,12]. A schematic draw of the ^{18}F levels intervening in the ^{17}O$(p,\alpha)\,^{14}$N reaction is shown in Fig. 2, together with the relevant Gamow energies for nova explosion and AGB stars.

Although the resonance energy and the (p,α) strength value of the 183-keV resonance have been largely studied by direct measurements, several issues concern the 65-keV and the subthreshold resonances parameters. For that reason we have performed a measurement to investigate the contribution of the 65-keV resonance to the reaction rate of ^{17}O$(p,\alpha)\,^{14}$N. In the following sections we first summarize previous results of direct measurements before outlining and discussing the results of our indirect approach using the Trojan Horse method (THM).

B. State of the art

The cross section of the ^{17}O$(p,\alpha)\,^{14}$N reaction has been the subject of several experimental investigations. Tables I and II summarize the main results obtained in the last 50 yr on the 65- and 183-keV resonances intervening in the ^{17}O-p interaction at astrophysical energies.

In the NACRE compilation of Angulo *et al.* [6], the contribution to the (p,γ) and (p,α) reaction rates from resonant levels up to ∼1.2 MeV had been evaluated. In particular, a $\omega\gamma_{p\gamma} = 5.9^{+1.9}_{-1.1} \times 10^{-11}$ eV has been recommended for the 65-keV resonance, while the upper limit of Landre *et al.* [12] has been used for Γ_p of the 183-keV level together with the upper limits on Γ_γ and Γ suggested in the work of Rolfs *et al.* ([16] and references therein). For the (p,α) channel, the compilation used the 65-keV resonance strength recommended in Blackmon *et al.* [14], while the 183-keV resonance strength has been calculated by using the upper limits given in Refs. [12,16].

Following the NACRE compilation, many works addressed the problem of the ^{17}O$+p$ cross sections at astrophysical energies, owing to their importance and the poor understanding of its trend.

TABLE I. Summary of the 65-keV resonance parameters intervening in the ^{17}O-p interaction as given in the literature.

Reference	E_X (keV)	Γ_p (eV)	Γ_α (eV)	Γ_γ (eV)	$(\omega\gamma)_{p\gamma}$ (eV)	$(\omega\gamma)_{p\alpha}$ (eV)
[15]	5662	8×10^{-8}	154	–	–	–
[16]	5668	$\leqslant 1.3 \times 10^{-9}$	–	0.5	–	–
[12]	5672.6 ± 0.3[a]	$7.1^{+4.0}_{-5.7} \times 10^{-8}$	130 ± 5[b]	1.4 ± 0.3[b]	–	–
[14]	–	$22 \pm 3_{\text{stat}} \pm 2_{\text{target}}{}^{+2}_{-1\ \text{beam}} \times 10^{-9}$	–	–	–	–
[17]	–	–	–	–	–	$\leqslant 8 \times 10^{-10}$
[6]	5672.57	22×10^{-9}[c]	130 ± 5[b]	–	$(5.9^{+1.9}_{-1.1}) \times 10^{-11}$	$(5.5^{+1.8}_{-1.0}) \times 10^{-9}$
[18]	–	$21 \pm 2 \times 10^{-9}$	–	–	–	–
[19,20]	–	–	–	–	$(1.6 \pm 0.3) \times 10^{-11}$	$(4.7 \pm 0.8) \times 10^{-9}$
[21]	–	$(19.0 \pm 3.2) \times 10^{-9}$	130 ± 5	0.44 ± 0.02	–	–

[a]Reference [22].
[b]Reference [23].
[c]Reference [14].

In the papers of Fox *et al.* [19,20], the proton-capture reaction on ^{17}O in the bombarding energy range of $E_p^{\text{lab}} =$ 180–450 keV was investigated and the previously undiscovered resonance at $E_R = 183$ keV was observed. Moreover, the resonance strength was deduced to be equal to $\omega\gamma_{p\gamma} = (1.2 \pm 0.2) \times 10^{-6}$ eV. With this new measured (p,γ) strength, the ^{17}O$+p$ reaction rate was reevaluated and an improved estimate for the (p,α) resonance strength was obtained [20]: At temperature lower than 2.0 GK the uncertainty in the ^{17}O$(p,\gamma)\,^{18}$F reaction rate was reduced from a few orders of magnitude down to ∼30% and the uncertainty in the ^{17}O$(p,\alpha)\,^{14}$N rates was reduced from an order of magnitude down to a factor ∼2.5. Moreover, in Fox's papers [19,20], the contribution of the $E_R = 65$ keV resonance on reaction rate was also taken into account both in (p,α) and (p,γ) reaction. In particular, they adopted the value $\omega\gamma_{p\alpha} = (4.7 \pm 0.8) \times 10^{-9}$ eV for the resonance strength in the ^{17}O$(p,\alpha)\,^{14}$N reaction reported in Ref. [18], which is slightly different from one reported in Ref. [14]. They also calculated the strength of the (p,γ) resonance, obtaining $\omega\gamma_{p\gamma} = (1.6 \pm 0.3) \times 10^{-11}$ eV. This latter value is significantly smaller, a factor ∼3.7, than that used by the NACRE compilation ($\omega\gamma_{p\gamma} = 5.9^{+1.9}_{-1.1} \times 10^{-11}$ eV) [6].

In 2007, three measurements have helped to significantly reduce the uncertainty of the ^{17}O$+p$ rates measuring the 183-keV resonance in the ^{17}O$(p,\alpha)\,^{14}$N reaction ([11,25,26] in Table II). The work of Chafa *et al.* [11] focused on the study of the 183-keV resonance. The corresponding α particles' angular distributions were measured for the ^{17}O$(p,\alpha)\,^{14}$N reaction and the strengths were measured for both (p,α) and (p,γ) channels, leading to $\omega\gamma_{p\alpha} = (1.6 \pm 0.2) \times 10^{-3}$ eV and $\omega\gamma_{p\gamma} = (2.2 \pm 0.4) \times 10^{-6}$ eV, in disagreement with the ones reported in Refs. [19,20]. Using their newly obtained $\omega\gamma_{p\alpha}$ value, the authors have well established the ^{17}O$(p,\alpha)\,^{14}$N rate below $T_9 = 1.5$, with uncertainties reduced from more than two orders of magnitude to 15% in the temperature range $T_9 = 0.1 - 0.4$.

In Newton *et al.* [25], the authors reported on a further measurement of the 183-keV resonance by using anodized oxygen targets instead of implanted targets as in Chafa *et al.* [11]. Their measured value $\omega\gamma_{p\alpha} = (1.66 \pm 0.17) \times 10^{-3}$ eV

TABLE II. Summary of the 183-keV resonance parameters intervening in the ^{17}O-p interaction as given in the literature.

Reference	E_X (keV)	Γ_p (eV)	Γ_α (eV)	Γ_γ (eV)	$(\omega\gamma)_{p\gamma}$ (eV)	$(\omega\gamma)_{p\alpha}$ (eV)
[16]	5785[a]	$\leqslant 1.4 \times 10^{-3}$	–	–	–	–
[24]	–	–	–	–	–	–
[12]	5786 ± 2.4	$\leqslant 2.8 \times 10^{-3}$	0.022[b]	0.022[b]	–	–
[6]	5786	$\leqslant 2.8 \times 10^{-3}$[,c]	0.022[b]	0.022[b]	–	–
[19,20]	–	–	–	–	$(1.2 \pm 0.2) \times 10^{-6}$	–
[11]	5789.8 ± 0.3	$(3.8 \pm 0.5) \times 10^{-3}$	6.8 ± 3.0	$(9.4 \pm 3.6) \times 10^{-3}$	$(2.2 \pm 0.4) \times 10^{-6}$	$(1.6 \pm 0.2) \times 10^{-3}$
[25]	–	–	–	–	–	$(1.66 \pm 0.17) \times 10^{-3}$
[26]	–	–	–	–	–	$(1.70 \pm 0.15) \times 10^{-3}$
[27]	–	–	–	–	$(1.67 \pm 0.12) \times 10^{-6}$	–
[28]	–	–	–	–	$(1.67 \pm 0.12) \times 10^{-6}$	–
[21]	–	$(4.00 \pm 0.24) \times 10^{-3}$	13.3 ± 5.5	$(9.6 \pm 3.6) \times 10^{-3}$	–	–

[a]Reference [29].
[b]Reference [30].
[c]Reference [12].

is in agreement with the result reported in Ref. [11], even if it does not solve the disagreement in the measured (p,γ) resonance strengths reported in Refs. [11,19,20].

The results by Moazen *et al.* [26] on the strength of the 183-keV resonance of $\omega\gamma_{p\alpha} = (1.70 \pm 0.15) \times 10^{-3}$ eV in the (p,α) channel were in good agreement with the results in Refs. [11,25]. Consequently, the derived reaction rate is in good agreement with that of Ref. [11].

The most recent compilation of Iliadis *et al.* [21] provides a detailed thermonuclear reaction-rate determination for both (p,α) and (p,γ) channels together with the nuclear physics input adopted by the authors (see Tables I and II for the 65- and 183-keV parameters, respectively, adopted in Ref. [21]). For this compilation the energy of the resonance at $E_R = 65.1 \pm 0.5$ keV has been calculated from the excitation energy $E_X = 5671.6 \pm 0.2$ keV reported in Ref. [11]. For the $E_R = 183$ keV resonance, the weighted average values of the energies and strengths measured by Refs. [11,25,26] were adopted. For the higher-energy resonances above $E_R = 500$ keV, the partial widths have been adopted from the R-matrix analysis (see Table 3 of [24]). The two-level interferences between the 1^- resonances at -2 and 65 keV and between the 2^- resonances at 183 and 1203 keV have been explicitly taken into account.

Recently, the 183-keV resonance strength has been measured with higher precision in a dedicated $^{17}\mathrm{O}(p,\gamma)^{18}\mathrm{F}$ measurement described in Scott *et al.* [27] and Di Leva *et al.* [28]. In these studies, the reaction cross section has been measured directly in a wide energy range, $E_{\mathrm{c.m.}} = 200$–370 keV, appropriate for hydrogen burning in classical novae. The authors extracted the value of $\omega\gamma_{p\gamma} = (1.67 \pm 0.12) \times 10^{-6}$ eV for the 183 keV, thus suggesting a reduction of a factor $\sim$4 for the corresponding $^{17}\mathrm{O}(p,\gamma)^{18}\mathrm{F}$ reaction rate.

Besides the above-mentioned direct measurements, the $^{17}\mathrm{O}(p,\alpha)^{14}\mathrm{N}$ reaction has been also investigated in Sergi *et al.* [31] by means of the THM. From such analysis, the value of $(3.66^{+0.76}_{-0.64}) \times 10^{-9}$ eV has been extracted for the 65-keV resonance strength. This value has been deduced by using the 183-keV resonance strength [11,25,26] as normalization values.

In this paper, we report on the detailed analysis of the experiment discussed in Ref. [31], as well as the analysis of a further experiment performed in 2008. Thanks to the most recent results of Iliadis *et al.* [21] and of Di Leva *et al.* [28], the (p,α) and (p,γ) THM rates are evaluated.

II. ELECTRON SCREENING: THE NEED FOR INDIRECT METHODS

Owing to the Coulomb barrier in the entrance channel, the cross section $\sigma(E)$ of a fusion reaction drops exponentially with decreasing center-of-mass energy E,

$$\sigma(E) = \frac{S(E)}{E}\exp(-2\pi\eta), \tag{3}$$

where η is the Sommerfeld parameter and $S(E)$ is the astrophysical S factor. The parametrization assumes that the Coulomb barrier is that resulting from bare nuclei, in s-wave and energies approaching zero. However, for nuclear reactions studied in the laboratory, the target nuclei and the projectiles are usually in the form of neutral atoms or molecules and ions, respectively. This means that the electron clouds partially shield nuclear charges, thus reducing the Coulomb suppression effect. This causes an increase of the cross section with respect to the case of bare nuclei, described by the enhancement factor $f_{\mathrm{enh}}(E)$ [32–34] given by

$$f_{\mathrm{enh}}(E) = \frac{\sigma_s(E)}{\sigma_b(E)} \approx \exp\left(\pi\eta\frac{U_e}{E}\right), \tag{4}$$

where $\sigma_s(E)$ and $\sigma_b(E)$ are the screened and bare-nucleus cross sections, namely, the cross section the particles would have if stripped of all the surrounding electrons and U_e is the electron screening potential. The presence of atomic electrons produces an enhancement of the cross section when the energy in the center-of-mass system approaches zero, which is not related to the nuclear interaction (e.g., subthreshold resonances) in the $^{17}\mathrm{O}$-p channel. In the case of the $^{17}\mathrm{O}+p$ interaction an increase of the cross section by a factor larger than 15% is expected at 65 keV [32].

Clearly, a good understanding of U_e is needed to calculate $\sigma_b(E)$ from Eq. (4). The effective cross section $\sigma_{\mathrm{pl}}(E)$ in the stellar plasma is connected to the bare nucleus cross section $\sigma_b(E)$ by the relation

$$\sigma_{\mathrm{pl}}(E) = \sigma_b(E) f_{\mathrm{pl}}(E) \approx \sigma_b(E)\exp(\pi\eta U_{\mathrm{pl}}/E), \tag{5}$$

where f_{pl} is the enhancing screening factor and U_{pl} is the electron screening potential in the stellar plasma. If $\sigma_b(E)$ is measured at ultralow energies and U_{pl} is estimated within the framework of the Debye-Huckel theory, it is possible estimate from Eq. (5) the effective cross section $\sigma_{\mathrm{pl}}(E)$ in the stellar plasma.

However, even in those few cases in which $\sigma_s(E)$ measurements have been performed at astrophysical energies, extrapolation from direct data at higher energies, where electron screening is negligible, is required to evaluate the bare-nucleus cross sections $\sigma_b(E)$. For these reasons, the so-called indirect methods have been introduced, aiming at accessing the low-energy astrophysical factor with no need of extrapolations. With the help of nuclear reaction theory, these processes allow us to extract information on astrophysically relevant reactions studying an alternative suitable reactions. Among these, the indirect THM [35–38] provides at present the only way to measure the energy dependence of the bare nucleus cross section down to the relevant ultralow energies, overcoming the main problems of direct measurements.

III. THE TROJAN HORSE METHOD

The THM was successfully applied to study several reactions [39–45] relevant to astrophysics. The method has proven particularly suited for acquiring information on charged as well as neutral-particle-induced reaction cross sections at astrophysical energies.

The basic idea of the THM is to extract the cross section in the low-energy region of a two-body reaction with significant astrophysical impact,

$$A + x \rightarrow b + B, \tag{6}$$

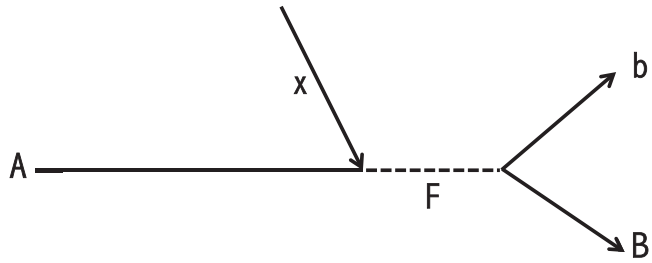

FIG. 3. Pole diagram of the $a + A \rightarrow s + b + B$ resonant QF process. Nucleus a breaks up into fragments x and s. The former is captured by A, leading to the formation of the compound system F, while s flies away without influencing either the $A + x \rightarrow F$ fusion or $F \rightarrow b + B$ decay.

from a suitable three-body reaction,

$$a + A \longrightarrow s + b + B. \tag{7}$$

This can be achieved by properly selecting the contribution to the total reaction yield coming from the quasifree (QF) direct reaction mechanism, where the Trojan Horse (TH) nucleus a, with its strong $x \oplus s$ cluster structure, breaks up inside the nuclear field of nucleus A.

This is demonstrated in Fig. 3: The impinging nucleus interacts with one of the clusters constituting the target (called *participant* x), while the residual nucleus does not participate in the reaction (*spectator* s). The latter is free from any effect owing to the interaction between the incoming nucleus and the participant, maintaining in the exit channel the same momentum distribution for the intercluster (x-s) motion it had inside a before the occurrence of QF breakup. Equivalently, the projectile nucleus may undergo breakup. If the bombarding energy E_A is chosen high enough to overcome the Coulomb barrier in the entrance channel of the three-body reaction (7), both Coulomb barrier and electron screening effects are negligible.

For resonant cases (see the Appendix for a general discussion on THM), the $a + A \rightarrow s + b + B$ reaction can be regarded as a two-step process, namely the stripping $a + A \rightarrow s + F$ to a resonant state in the compound system F_i, which later decays to the $b + B$ channel [46,47]. Correspondingly, the cross section of such process can be factorized and the resonance parameters can be deduced from the experimental TH data. In particular, if $\mathbf{k}_{ij} = (m_j\mathbf{k}_i - m_i\mathbf{k}_j)/m_{ij}$ is the relative momentum of the particles i and j ($\mathbf{k}_i$ and m_i are the momentum and the mass of the ith particle, respectively), the TH double differential cross section can be written as [46,48–50]

$$\frac{d^2\sigma^{\mathrm{TH}}}{d\Omega_{\mathbf{k}_{sF}} dE_{bB}} = \frac{1}{2\pi} \frac{\Gamma_{bB}(E_{bB})}{\left(E_{bB} - E_{R_{bB}}\right)^2 + \frac{1}{4}\Gamma^2(E_{bB})} \frac{d\sigma_{(a+A\rightarrow s+F)}}{d\Omega_{\mathbf{k}_{sF}}}, \tag{8}$$

where $\frac{d\sigma_{(a+A\rightarrow s+F)}}{d\Omega_{\mathbf{k}_{sF}}}$ is the differential cross section for the stripping $A(a,s)F$ reaction populating the F_i resonant state with resonance energy $E_{R_{bB}}$. $\Gamma_{bB}(E_{bB})$ is the partial resonance width for the $F \rightarrow b + B$ decay; Γ is the total resonance width. Finally, $E_{ij} = k_{ij}^2/(2\mu_{ij})$ is the relative kinetic energy of the particle i and j, with μ_{ij} their reduced mass (see the Appendix for more details).

We apply the THM to determine the cross section of the $^{17}\mathrm{O}(p,\alpha)^{14}\mathrm{N}$ reaction by selecting the QF contribution to the $^2\mathrm{H}(^{17}\mathrm{O}, ^{14}\mathrm{N}\,\alpha)n$ reaction. The proton is brought inside the nuclear field of $^{17}\mathrm{O}$, while the neutron acts as a spectator to the $^{17}\mathrm{O}(p,\alpha)^{14}\mathrm{N}$ QF reaction. The deuteron was used as the TH nucleus because of

(i) its p-n structure;
(ii) its relative low binding energy (∼2.2 MeV);
(iii) its well-known radial wave function for the p-n relative motion, mainly occurring in the s wave [51,52]. The deuteron momentum distribution for the p-n relative motion is given by the Hulthén wave function in momentum space, having its maximum at 0 MeV/c and a full width at half maximum (FWHM) of ∼60 MeV/c.

IV. THE EXPERIMENT

The study of the $^{17}\mathrm{O}(p,\alpha)\,^{14}\mathrm{N}$ via the THM application was carried out in two experiments: the first one at the Laboratori Nazionali del Sud (LNS) in Catania (Italy) and the second one at the Nuclear Science Laboratory (NSL) of the University of Notre Dame (USA). In the LNS experiment, the SMP Tandem Van de Graaff accelerator provided a 41-MeV $^{17}\mathrm{O}$ beam, with a spot size on target of about 1.5 mm and intensities up to 2–3 nA, impinging on a deuterated polyethylene target (CD_2) of about 150 μg/cm^2 placed at 90° with respect to the beam axis. In the NSL experiment, a beam energy of 43.5 MeV and a target thickness of 170 μg/cm^2 were used. The angles and the energies of the ejected α and $^{14}\mathrm{N}$ were detected in coincidence by using six single-area, resistive-readout, position-sensitive silicon detectors (PSDs) with spatial resolution of 0.5 mm that were mounted symmetrically with respect to the beam direction. The neutron was not detected in these experiments, and its energy and emission angle were reconstructed from the momenta of the detected particles. The PSD detectors covered the angular ranges in the laboratory reference system 5.1°–10.1° ($\mathrm{PSD}_{1,4}$), 13.8°–21.2° ($\mathrm{PSD}_{2,5}$), and 21.3°–28.7° ($\mathrm{PSD}_{3,6}$) in the LNS experiment and 5.0°–10.0° ($\mathrm{PSD}_{1,4}$), 13.1°–18.1° ($\mathrm{PSD}_{2,5}$), and 23.8°–28.8° ($\mathrm{PSD}_{3,6}$) in the NSL experiment. In Fig. 4, a schematic drawing of the detection setup is shown.

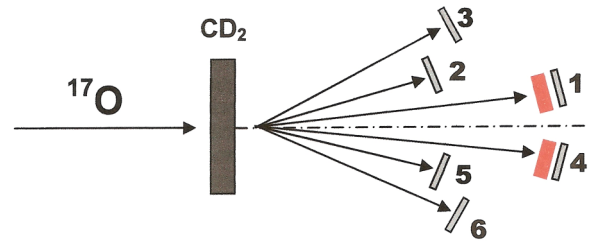

FIG. 4. (Color online) Experimental setup adopted for the study of the $^2\mathrm{H}(^{17}\mathrm{O},\alpha\,^{14}\mathrm{N})n$ reaction. The displacement of the detectors assures the covering of the QF angular region.

In front of the two forward PSDs, two ionization chambers (ICs) were used as ΔE detectors to discriminate the impinging ^{14}N reaction products from ^{14}C coming from the ^{2}H(^{17}O,α^{14}C)p reaction. The ICs were filled with 60 mbar of isobutane gas and were closed on both sides by 1.5-μm-thick Mylar foil windows. The gas pressure inside the ICs was selected to yield a high-enough signal-to-noise ratio. No energy threshold was needed for the ΔE detector on ^{14}N detection. The ^{14}N particles were emitted with energies higher than 18 MeV, thus exceeding the energy threshold of our telescope system ($\sim$11 MeV) for ^{14}N detection. An energy threshold of about 2.5 MeV was introduced on α-particle detection in the same telescope. However, no ΔE detectors were placed in front of detectors devoted to the α-particles detection, PSD_2, PSD_3, PSD_5, and PSD_6. This was necessary to measure the α particles over the entire energy range down to zero energy.

Detectors covered the angular region where the contribution of the QF reaction mechanism is expected to be maximum. Indeed, because the TH nucleus a is a deuteron, the n-p relative motion essentially takes place in the s wave; thus, the corresponding momentum distribution has a maximum for $p_s = 0$ MeV/c. Thanks to the use of PSDs, we could span momentum values of the undetected neutron between 0 MeV/c and $\sim$100 MeV/c. This ensures that the bulk of the QF contribution for the breakup process of interest falls inside the investigated regions. The angles corresponding to the condition of maximum QF contribution (that is, $p_s = 0$ MeV/c in the case of deuteron) are known as *QF angles*.

Energy and position signals, as well as coincidence information, were processed by standard electronics. Coincidences among either one of the two forward PSDs and one of the three placed on the opposite side with respect to the beam axis were recorded by the data-acquisition system.

At the initial stage of the measurement, masks with a number of equally spaced slits were placed in front of each PSD to perform position calibration. The angle of each slit with respect to the beam direction was measured by means of an optical system, making it possible to establish a correlation between position signal from the PSDs and detection angle of the impinging particles.

In the LNS experiment, detectors were calibrated at low en-ergies using a three-peak α source (^{239}Pu at 5.16 MeV, ^{241}Am at 5.48 MeV, ^{244}Cm at 5.80 MeV). At higher energies, the calibration was based on elastic scattering measurements of ^{6}Li on ^{197}Au and a ^{12}C. The ^{6}Li beam energies were 35.9 and 14.8 MeV. Moreover, additional runs were performed to measure the ^{12}C particle from the elastic scattering ^{17}O + ^{12}C at $E_{\rm beam} = 41$ MeV. In the NSL experiment energy calibration was performed by measuring the ^{12}C elastic scattering on gold at beam energies from 15 to 40 MeV and by using the α elastic scattering on gold at energies between 5 and 22 MeV. In this way an accurate calibration of PSD_1, PSD_4 was obtained. The IC was calibrated by taking the differences of the residual energies measured by PSD_1 and PSD_4 when the IC was empty and filled with isobutane at the working pressure, respectively. The total kinetic energy of the detected particles was reconstructed off line, taking into account the energy loss in the target and in the entrance and exit windows of the ICs and in other dead layers.

V. DATA ANALYSIS

A. Reaction channel selection

To disentangle the contribution of the ^{2}H(^{17}O,α^{14}N)n reaction from background reaction products, the procedure discussed in Refs. [31,38,53], for instance, was followed. $Z = 7$ particles were selected with the standard $\Delta E - E$ technique in telescopes 1 and 4. A typical $\Delta E - E$ 2D plot is shown in Fig. 5, where the $Z = 8$, $Z = 7$, and $Z = 6$ loci are marked. However, IC energy resolution (about 10%) was not enough to disentangle different isotopes, allowing for discrimination of Z only. Moreover, to keep detection thresholds as low as possible, no ΔE detectors were placed in front of the detectors optimized for α particle detections. Finally, because the third particle remains undetected, its kinematical variables have been then reconstructed under the assumption that its mass is 1 (neutron mass).

As a first test, the experimental Q-value spectrum was reconstructed for the selected $Z = 7$ events by means of the momentum and energy conservation. The result is displayed in Fig. 6, where a well-defined peak appears centered at about -1 MeV. This is in agreement with the theoretical ^{2}H(^{17}O,α^{14}N)n three-body reaction Q value, $Q_{\rm th} = -1.033$ MeV. No other peak is apparent, proving that reactions other than the THM one are not significantly populated, the upper limit for background being about 3%. The agreement, within the experimental uncertainties, is a signature of a good detector calibration. Because the ^{2}H(^{17}O,α^{14}N)n reaction has three particles in the exit channel, events from such reaction gather along a well-defined kinematic locus. By selecting the locus of interest, a kinematic identification of the reaction channel

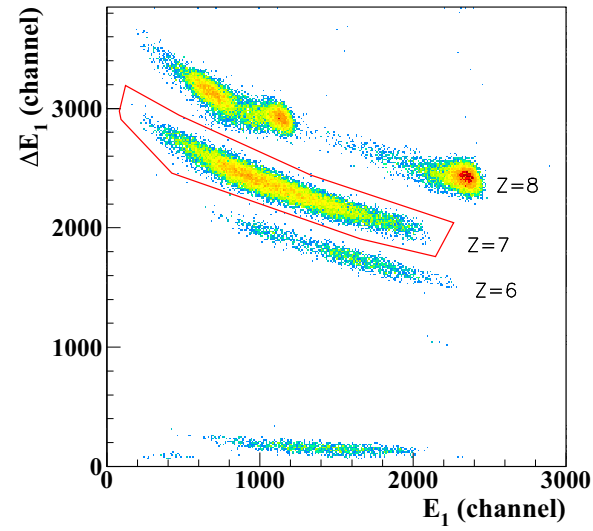

FIG. 5. (Color online) ΔE-E matrix for the gas detector used as a first stadium of the telescopes formed with the PSD_1. The telescopes were devoted to the identification of $Z = 7$ particles, which are selected with a graphical cut (red lines).

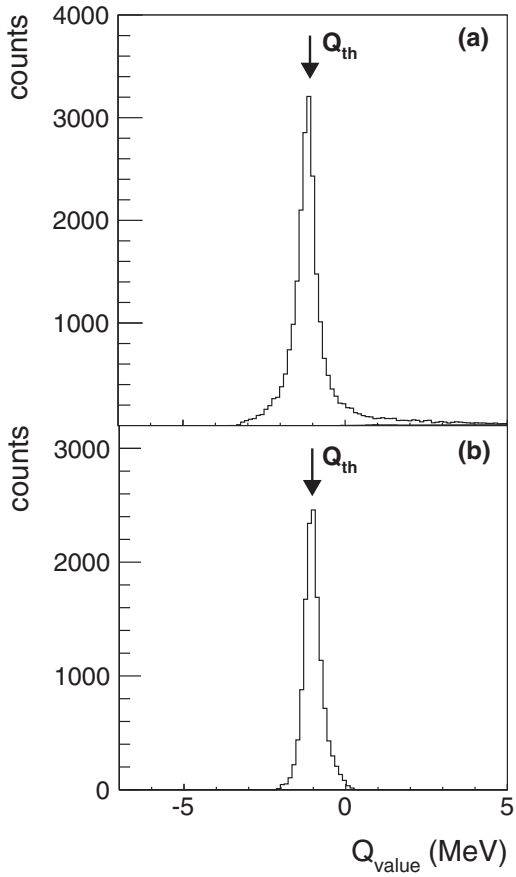

FIG. 6. Experimental Q-value spectra for LNS (a) and NSL (b) experiments. A single peak shows up in both spectra, centered at about -1.0 MeV, corresponding to the ^{2}H(^{17}O,α^{14}N)n channel. The black arrows correspond to the theoretical Q value, $Q_{\rm th} = -1.033$ MeV.

and, consequently, of the detected reaction products can be performed. For this purpose, we have plotted the energies measured in each detector pair against each other, gating on the $Z = 7$ locus in the ICs. For instance, Fig. 7 shows the $E_{14_{\rm N}}$ vs E_{α} 2D spectrum for $\theta_{14_{\rm N}} = 6.0^{\circ} \pm 0.5^{\circ}$ and $\theta_{\alpha} = 21.0^{\circ} \pm 0.5^{\circ}$. By comparison with the corresponding three-body kinematic calculation (black circles) it turns out that a single reaction channel contributes to the $E_{14_{\rm N}} - E_{\alpha}$ correlation plot and the observed kinematic locus corresponds to the one for the ^{2}H(^{17}O,α^{14}N)n three-body reaction. Similar results are obtained for other angular couples and coincident detectors.

Events inside the experimental Q-value peak were selected for further analysis.

B. Selection of the QF reaction mechanism

Once the three-body reaction of interest has been selected, the next step of a TH analysis consists of discrimination and selection of the QF contribution. This procedure is crucial for the following application of the THM because the equations described in Sec. III can be applied to QF events only. In fact, they are valid only under the assumption that particle s, namely the neutron, acts as a spectator to the A-x

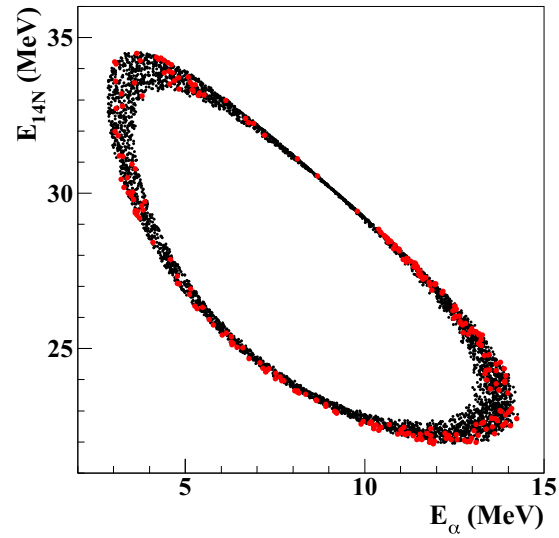

FIG. 7. (Color online) Experimental kinematic locus (red circles) for the three-body ^{2}H(^{17}O,α^{14}N)n reaction induced at $E_{\rm beam} = 41$ MeV and for $\theta_{14_{\rm N}} = 6.0^{\circ} \pm 0.5^{\circ}$ and $\theta_{\alpha} = 21.0^{\circ} \pm 0.5^{\circ}$ (LNS experiment), superimposed onto the simulated kinematical locus (black circles) as discussed in the text. The spectra are relative to the events measured in coincidence among PSD$_1$-PSD$_5$ detectors.

interaction. Therefore, it is necessary to evaluate the presence of other reaction mechanisms feeding the same particles in the exit channel such as sequential decay (SD) and direct breakup. To study the reaction mechanisms through which the ^{2}H(^{17}O,α^{14}N)n process takes place, relative energies for any two of the three final particles were calculated event by event. For the LNS experiment, the correlation plots for the relative energies of the particles in the exit channel $E_{^{14}{\rm N}\text{-}\alpha}$ vs $E_{\alpha\text{-}n}$ and $E_{^{14}{\rm N}\text{-}n}$ vs $E_{\alpha\text{-}n}$ are shown in Figs. 8(a) and 8(b), respectively. Similar results were obtained in NSL measurement. In this plot [Fig. 8(a)], events coming from the decay of an excited state of ^{18}F would gather along a locus parallel to the horizontal axis, as the excited-state energy is independent of the α-n relative energy. The same considerations apply to decays from ^{15}N excited states [Fig. 8(b)]. If ^{5}He states were populated, instead, events should gather along a locus parallel to the y axis as the ^{5}He excitation energy is independent of the ^{14}N-α and ^{14}N-n relative energies. From these considerations, we deduce that the horizontal loci of Fig. 8(a) correspond to the population of ^{18}F excited levels. Conversely, in both panels of Fig. 8 there is no evidence of excited levels in $E_{\alpha-n}$ variable correlated to the excited state of ^{5}He compound nucleus. Therefore, we are confident that the ^{2}H(^{17}O,α^{14}N)n reaction does not proceed through the $^{2}{\rm H} + {}^{17}{\rm O} \rightarrow {}^{5}{\rm He} + {}^{14}{\rm N} \rightarrow {}^{4}{\rm He} + {}^{14}{\rm N} + n$ two-step process. Similarly, the $^{2}{\rm H} + {}^{17}{\rm O} \rightarrow {}^{4}{\rm He} + {}^{15}{\rm N} \rightarrow {}^{4}{\rm He} + {}^{14}{\rm N} + n$ two-step reaction would lead to the formation of an intermediate ^{15}N excited system. In Fig. 8(a), the presence of excited states of ^{15}N is confirmed by the occurrence of two loci at fixed ^{14}N-n relative energies of 2 and 2.5 MeV, thus constituting an SD process contributing to the total reaction yield. For such a reason, a quantitative analysis of the presence of SD processes and QF mechanism was performed by studying the coincidence yield of the

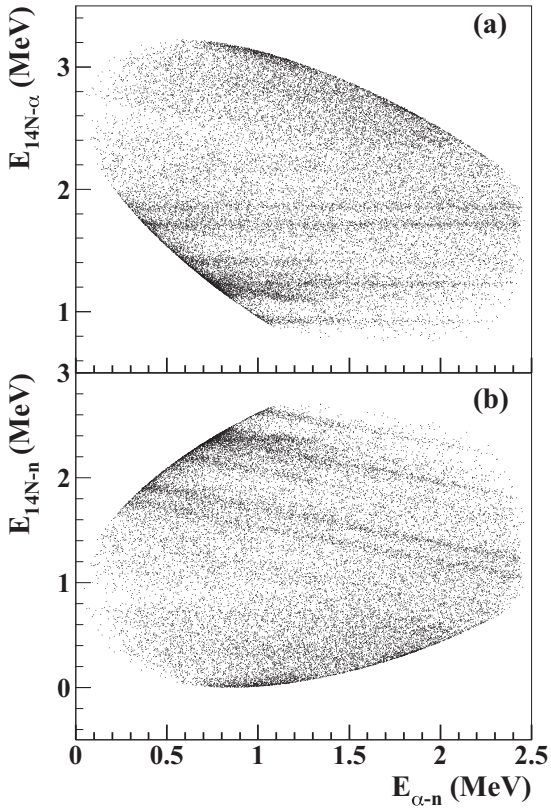

FIG. 8. (a) $E_{^{14}\mathrm{N}\text{-}\alpha}$ vs $E_{\alpha\text{-}n}$ 2D plot. The presence of horizontal loci at $E_{^{14}\mathrm{N}\text{-}\alpha} = 1.26$, 1.37, 1.67, and 1.82 MeV demonstrates the feeding of the $^{14}\mathrm{N}+\alpha+n$ channel through the population of the $^{18}\mathrm{F}$ excited states at $E_X = 5.672$ MeV ($J^\pi = 1^-$), $E_X = 5.786$ MeV ($J^\pi = 2^-$), $E_X = 6.094$ MeV ($J^\pi = 4^-$), and $E_X = 6.108$ MeV ($J^\pi = 1^+$) (unresolved) and $E_X = 6.240$ MeV ($J^\pi = 3^-$) and $E_X = 6.242$ MeV ($J^\pi = 3^-$) (unresolved). Moreover, the horizontal loci at $E_{^{14}\mathrm{N}\text{-}\alpha} = 1.09$ and 1.19 MeV corresponded to three subthreshold levels (two of them are unresolved) at $E_X = 5.502$ ($J^\pi = 3^-$), $E_X = 5.603$ ($J^\pi = 1^+$), and $E_X = 5.605$ ($J^\pi = 1^-$) MeV. (b) Similarly, the $E_{^{14}\mathrm{N}\text{-}n}$ vs $E_{\alpha\text{-}n}$ 2D plot shows the occurrence of a SD process taking place by populating $^{15}\mathrm{N}$ excited states at E_X from 13 and 13.35 MeV determining the appearance of horizontal loci at ∼2.0 and ∼2.5 MeV.

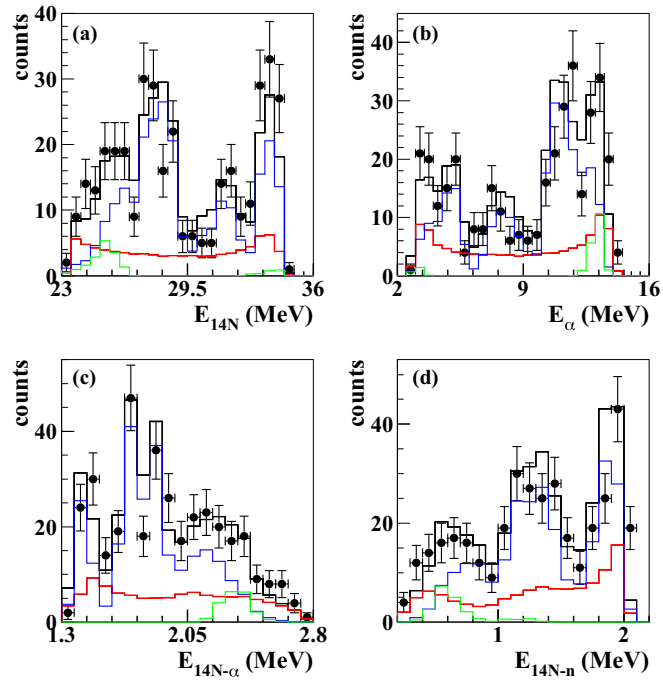

FIG. 9. (Color online) $^{2}\mathrm{H}(^{17}\mathrm{O},\alpha^{14}\mathrm{N})n$ yield as a function of $E_{^{14}\mathrm{N}}$, E_α, $E_{^{14}\mathrm{N}\text{-}\alpha}$, and $E_{^{14}\mathrm{N}\text{-}n}$ for $\theta_{^{14}\mathrm{N}} = 6.0^\circ \pm 0.5^\circ$ and $\theta_\alpha = 21.0^\circ \pm 0.5^\circ$. In panel (a), the black line is a fit of the coincidence yield obtained by taking into account SD (green line), QF (blue line), as well as combinatorial background (red line) contributions summed incoherently (see text for more details). In panels (b)–(d), the data are represented as a function of other variables. A remarkable agreement between the data and the incoherent sum (black lines) obtained using the same parameters for the SD (green line), QF (blue line), and combinatorial background contributions (red line) is clearly shown for all of the variables.

three-body reaction as a function of different variables for fixed values of $\theta_{^{14}\mathrm{N}}$ and θ_α. The spectra were fitted by adding incoherently the contributions of SD and QF reaction calculations based on Monte Carlo simulations, leaving the relative weights of the cited contributions as free fitting parameters. The coincidence yields were described by using Eq. (A1) in the Appendix for the QF process while the resonant $^{18}\mathrm{F}$ and $^{15}\mathrm{N}$ contributions were given by a Gaussian shape because of the present experimental resolution of about $\epsilon = 20$ keV. For each fixed angular pair ($\theta_{^{14}\mathrm{N}}$, θ_α), the fit was performed for the $E_{^{14}\mathrm{N}}$ spectrum, and the obtained weights for the SD and QF processes were used to reproduce the E_α, $E_{^{14}\mathrm{N}\text{-}\alpha}$, and $E_{^{14}\mathrm{N}\text{-}n}$ spectra without any further adjustment of the deduced fitting parameters. For instance, Fig. 9(a) shows the fit of the coincidence yield as a function of $E_{^{14}\mathrm{N}}$ for the QF angular couple $\theta_{^{14}\mathrm{N}} = 6.0^\circ \pm 0.5^\circ$ and $\theta_\alpha = 21.0^\circ \pm 0.5^\circ$. The black line represents the results of the fit, the red line shows the combinatorial background contribution, the blue line represents the contribution of QF owing to the population of the $^{18}\mathrm{F}$ resonant levels ($E_X = 5.672$, 5.786, 6.094, 6.108, 6.240 MeV and $E_X = 6.242$ MeV), while the green line shows the contributions of SD owing to the population of $^{15}\mathrm{N}$ states at ∼2.5 MeV. In Figs. 9(b) and 9(d), the coincidence yield as a function of E_α, $E_{^{14}\mathrm{N}\text{-}\alpha}$, and $E_{^{14}\mathrm{N}\text{-}n}$ is compared with the incoherent sum (black lines) of the Monte Carlo calculations for SD and QF processes, weighted with the parameters obtained from the fit of Fig. 9(a). The agreement between data and simulation gives us confidence in the accuracy of the fit. As before, the contribution of the combinatorial background is represented by a red line, while the blue and the green lines represent the QF contribution owing to the population of $^{18}\mathrm{F}$ resonant levels and SD contributions coming from population of $^{15}\mathrm{N}$ states, respectively. Similar results are obtained for other angular pairs. On average, the fit of the coincidence yields returns a 29% contribution of the combinatorial background, a 66% contribution of the QF mechanism owing to the population of the $^{18}\mathrm{F}$ resonant levels at the QF angular pairs, and a 5% contribution of SD owing to the population of $^{15}\mathrm{N}$ states. Under these conditions, the SD proceeding through $^{15}\mathrm{N}$ states gives a negligible contribution to the coincidence yield at

α-^{14}N relative energies corresponding to the region of interest for astrophysics, i.e., around $E_{^{14}\text{N-}\alpha} = 1.2$ MeV.

A complementary way to discriminate between SD and QF events is to study the reaction yield as a function of the neutron momentum p_n. In the QF hypothesis, the cross section of the three-body reaction is related to the spectator momentum distribution through Eq. (A1) given in the Appendix and discussed in Refs. [38,54]. Thus, when approaching the QF kinematic condition, where the momentum distribution has a maximum, the reaction yield should be enhanced, if corrected for phase-space population effects and neglecting resonances in the two-body cross section [38,54]. In the present case, because the momentum distribution of the n-p system inside deuteron has a maximum for $p_n = 0$ MeV/c, an enhancement of the cross section is expected when approaching zero neutron momentum values. This represents a necessary condition for the occurrence of the QF mechanism, marking the presence of a modulation of the TH cross section by the neutron momentum distribution inside the deuteron. For this purpose, the behavior of the coincidence yield spectra as a function of $E_{\text{c.m.}}$ was reconstructed for different ranges of neutron momentum. Here $E_{\text{c.m.}}$ is the ^{17}O-p relative kinetic energy, related to the $E_{^{14}\text{N-}\alpha}$ relative energy by the energy conservation law,

$$E_{\text{c.m.}} = E_{^{14}\text{N-}\alpha} - Q_2, \tag{9}$$

where $Q_2 = 1.192$ MeV is the Q value of the ^{17}O(p,α)^{14}N reaction. In detail, three different momentum ranges, namely $|\vec{p}_n| \leqslant 30$ MeV/c, 30 MeV/$c \leqslant |\vec{p}_n| \leqslant 60$ MeV/c, and 60 MeV/$c \leqslant |\vec{p}_n| \leqslant 90$ MeV/c, have been selected, as shown in the three panels of Fig. 10. To remove phase-space effects, the coincidence yield was divided by the kinematic factor KF [see Eq. (A1) in the Appendix]. Moving from small p_n values [$|\vec{p}_n| \leqslant 30$ MeV/c, panel (a)] to larger values (60 MeV/$c \leqslant |\vec{p}_n| \leqslant 90$ MeV/c), the corrected coincidence yield decreases by a factor of ~2.5 in correspondence to the ^{18}F resonances at 65 and 183 keV. This procedure reveals a strong correlation between the coincidence yield and the neutron momentum p_n, a necessary condition for the occurrence of the QF reaction mechanism, as discussed before. Similar results are obtained for different detector couples and for both the LNS and NSL measurements.

To make the previous discussion more quantitative, the study of the neutron momentum distribution inside deuteron also was performed. In fact, the QF processes are characterized by the presence of a particle in the exit channel that acts as a spectator. This means that in the exit channel the spectator particle—the neutron in this case—must maintain the same momentum distribution that it had before the interaction of the oxygen projectile with deuteron. For this reason the shape of the experimental momentum distribution represents a very sensitive observable to the reaction mechanism. To reconstruct the experimental p_n distribution, the energy-sharing method [55] was applied to each pair of coincidence detectors, selecting a narrow $E_{\text{c.m.}}$ relative energy window, $\Delta E = 100$ keV, at the top of the 183-keV resonant peak corresponding to the 5.787-MeV state in ^{18}F, which is clearly visible in Fig. 10.

Within such restricted ^{17}O-p relative energy ranges, the differential two-body cross section of the ^{17}O-p reaction, can

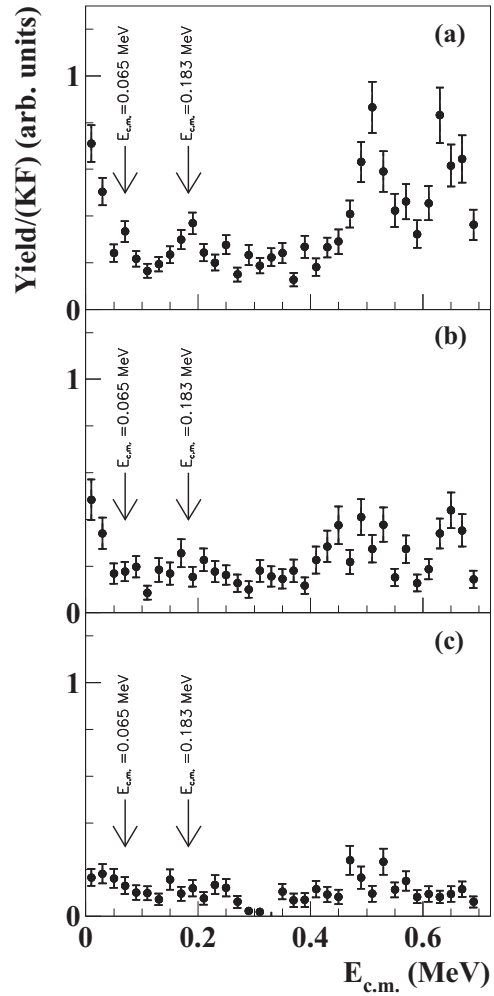

FIG. 10. PSD$_1$ − PSD$_5$ coincidence yield (LNS experiment), extracted for different neutron momentum p_n ranges: $|\vec{p}_n| \leqslant 30$ MeV/c (a), 30 MeV/c $\leqslant |\vec{p}_n| \leqslant 60$ MeV/c (b) and finally 60 MeV/c $\leqslant |\vec{p}_n| \leqslant 90$ MeV/c (c). In each case, the coincidence yield is divided by the kinematical factor to remove phase-space effects, thus the trend of the cross section as a function of $E_{\text{c.m.}}$ and of p_n only is left out.

be considered to be almost constant; thus, the experimental p_n momentum distribution is given in arbitrary units by inverting Eq. (A1) (Appendix),

$$|\phi(\vec{p}_n)|^2 \propto \left[\frac{d^3\sigma}{d\Omega_\alpha d\Omega_{^{14}\text{N}} dE_{\text{c.m.}}}\right][KF]^{-1}, \tag{10}$$

where KF is the kinematical factor containing the final-state phase-space factor and it is a function of the masses, momenta, and angles of the outgoing α, ^{14}N, and n particles [54]. The experimental p_n momentum distribution is then compared with the theoretical one, given in terms of a Hulthén wave function in momentum space in the plane-wave impulse approximation (PWIA),

$$|\phi(\vec{p}_n)|^2 = \frac{1}{\pi}\sqrt{\frac{ab(a+b)}{(a-b)^2}}\left[\frac{1}{a^2+p_n^2} - \frac{1}{b^2+p_n^2}\right], \tag{11}$$

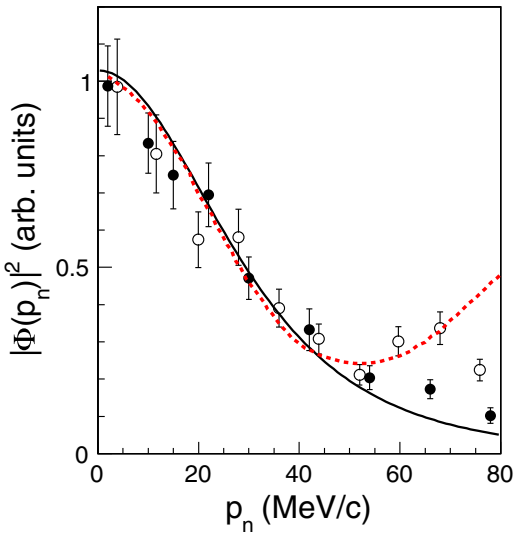

FIG. 11. (Color online) Experimental momentum distributions (solid dots for LNS experiment and open dots for NSL experiments) compared with the theoretical ones, given by the square of the Huthén function (black line) in the PWIA and by the DWBA momentum distribution evaluated by means of FRESCO code (red dotted line).

with parameters $a = 0.2317$ fm^{-1} and $b = 1.202$ fm^{-1} [56] for the deuteron.

The two experimental momentum distributions $|\phi(\vec{p}_n)|^2$, obtained in arbitrary units for both measurements, are displayed in Fig. 11 by solid black dots (LNS experiment) and by open circles (NSL experiment). The theoretical momentum distribution has been scaled to the experimental data by multiplying it for a constant term, fitted to the experimental LNS (o NSL) data. The result is shown in Fig. 11 as a black solid line. The good agreement, within the experimental errors, between the experimental data and the theoretical momentum distribution represents the experimental evidence that the neutron acted as a spectator during the breakup that occurred in the $^2\mathrm{H} + {}^{17}\mathrm{O} \rightarrow \alpha + {}^{14}\mathrm{N} + n$ reaction. These results are also in agreement with the conclusion of Ref. [57]. Indeed, if the transferred momentum is calculated for the present kinematical conditions following the prescription in Ref. [58], a FWHM of $\sim$60 MeV/c is expected, in agreement with the present experimental result, 61 ± 5 MeV/c. The experimental FWHM essentially coincides with the asymptotic one as the transferred momentum is comparatively large (see Ref. [58] for details).

To check whether the simple PWIA approach gives an accurate description of the n-p momentum distribution, the momentum distribution data were also compared with the DWBA distribution (red dotted line in Fig. 11) evaluated by means of the FRESCO code [59]. In the calculation, optical potential parameters adjusted from the Perey and Perey compilation [60] were adopted. From the comparison between the two theoretical approaches, we can state that a good agreement between DWBA and PWIA is present within the experimental uncertainties for a neutron momentum interval $|\vec{p}_n| \leqslant 30$ MeV/c. Such an agreement means that the QF mechanism is present and dominant in the $|\vec{p}_n| \leqslant 30$ MeV/c range. For this reason the further data analysis was performed on events falling inside this momentum window, allowing us to apply the PWIA without introducing significant model errors [61].

VI. RESULTS

A. Cross section of the ^{2}H(^{17}O,α ^{14}N)n reaction

To obtain the cross section for ^{2}H(^{17}O,α ^{14}N)n, we use the double differential TH cross section given by Eq. (8), which was obtained by integration over the solid angle $\Omega_{\alpha-{}^{14}N}$. The resulting ^{2}H(^{17}O,α ^{14}N)n reaction cross section is shown in Fig. 12 as solid dots for both the LNS (a) and the NSL experiments (b).

Here the vertical error bars arise from statistical uncertainty (about 20%, on the average), the horizontal error bars represent the integration energy bin, while the solid line represents the fit of the two-body cross section. In the fit, the combinatorial background is fitted using a straight line, while the resonant part is described by the incoherent sum of three Gaussian functions to account for the dominant energy resolution effects intervening in the present experiment ($\epsilon \sim 20$ keV). The quoted energy resolution of about 20 keV is the result of the propagation of the energy and angular straggling, affecting the measured quantities, on the $E_{^{14}\mathrm{N}\text{-}\alpha}$ variable intervening in the calculation of $E_{\mathrm{c.m.}}$ by Eq. (A2) in the Appendix. Thus, the experimental width reflects the effects

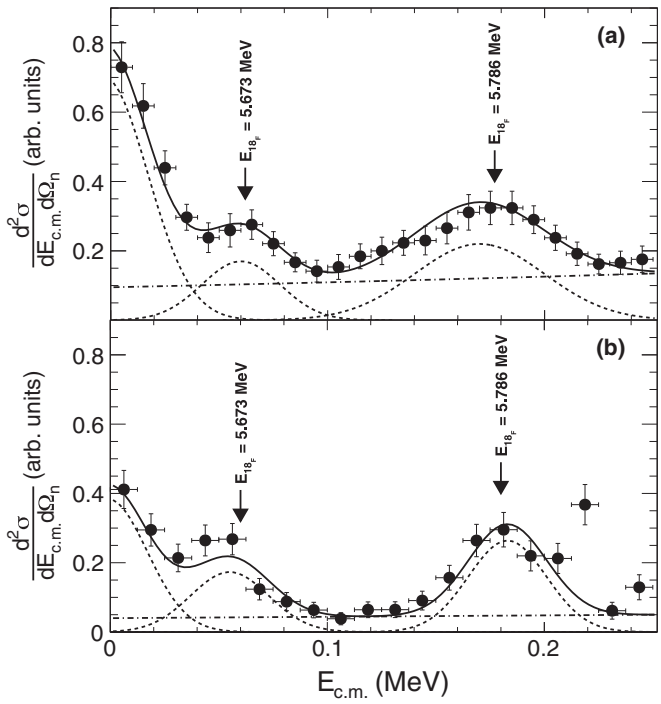

FIG. 12. Cross section of the TH reaction (solid circles) for the LNS (a) and NSL (b) experiments. The solid line represents the result of a fit including three Gaussian curves and a first-order polynomial to take into account the combinatorial background contribution to the cross section.

TABLE III. Summary of the experimental parameters for the two resonance levels in ^{18}F for the ^{17}O$(p,\alpha)^{14}$N reaction extracted as described in the text. The quoted errors for the two peak values N_1 and N_2 include statistical contribution ("stat."), background subtraction ("back."), and correlation between resonances ("corr."), as explained in the text.

Experiment	N_1	N_2
LNS	$0.1700 \pm 0.0250_{\text{stat.}} \pm 0.0040_{\text{back.}} \pm 0.0003_{\text{corr.}}$	$0.2200 \pm 0.0310_{\text{stat.}} \pm 0.0060_{\text{back.}} \pm 0.0002_{\text{corr.}}$
NSL	$0.1730 \pm 0.0290_{\text{stat.}} \pm 0.0040_{\text{back.}} \pm 0.0003_{\text{corr.}}$	$0.2640 \pm 0.0340_{\text{stat.}} \pm 0.0070_{\text{back.}} \pm 0.0002_{\text{corr.}}$

of the energy resolution that can be considered the same for all the observed resonances in the 0–250 keV energy range.

As extensively described in Refs. [31,47], the experimental THM cross section for the ^{2}H(^{17}O,α^{14}N)n QF process is given by

$$\frac{d^2\sigma}{dE_{\text{c.m.}}d\Omega_n} = \sum_{i=1}^{3} N_i \times \exp\left[-\frac{1}{2}\left(\frac{E_{\text{c.m.}} - E_{R_i}}{\epsilon}\right)^2\right] + a_0 + a_1 E_{\text{c.m.}}, \quad (12)$$

where a first-order polynomial has been added to account for combinatorial background. Equation (12) is obtained by folding the ideal resolution THM cross section, Eq. (8), with the detector response function that can be approximated by a Gaussian function whose width is fixed by the experimental standard deviation, $\epsilon = 20$ keV. In addition, in Eq. (12), E_{R_i} represent the resonance energies, $\epsilon = 20$ keV is the experimental energy resolution mentioned above, and the N_i parameters represent the TH resonance strengths, namely [47],

$$N_i = 2\pi \mathcal{N}_i \sigma_{R_i}(\theta) \frac{\Gamma_{(\alpha^{14}N)_i}(E_{R_i})}{\Gamma_i(E_{R_i})}. \quad (13)$$

Here $\mathcal{N}_i = 1/\sqrt{2\pi}\epsilon_i$ is the Gaussian normalization constant (we can take $\epsilon_i = \epsilon$ being the energy resolution constant), $\sigma_{R_i}(\theta)$ the direct transfer reaction cross section for the binary reaction $^{17}\text{O} + d \rightarrow {}^{18}\text{F}_i + n$ populating the ith resonant state in ^{18}F with the resonance energy E_{R_i} and $\Gamma_{(\alpha^{14}\text{N})_i}(E_{R_i})$ the partial widths for the $^{18}\text{F} \rightarrow \alpha + {}^{14}\text{N}$ decay channel of the ith excited state in ^{18}F and $\Gamma_i(E_{R_i})$ the total width of the ith resonance.

Even if two noninterfering resonances and two subthreshold states are populated in the covered energy range, the sum in Eq. (12) is limited to three energy states. In fact, because of the experimental energy resolution, the two subthreshold states, corresponding to the $E_X = 5.603$ MeV and $E_X = 5.605$ MeV states of ^{18}F [13], were not well separated.

The fits were performed to extract the peak values N_i of the two resonances with their statistical errors. In such a procedure, no interference effect was taken into account because of its negligible contribution. Indeed, for extracting the 65-keV resonance strength, the THM approach needs only to determine the experimental areas under the 65- and the 183-keV resonances, because these values are not significantly changed by interference effects. By using the two-level approximation given in Ref. [11] we have verified that the interference effect introduces a change smaller than 0.1% in our calculation. Moreover, the uncertainty owing to the combinatorial background subtraction, as well as the uncertainty owing to the peak-value correlation in the fits, were taken into account, as reported in Ref. [31]. In detail, the combinatorial background was evaluated using the procedure described in Fig. 9. Because the energy range considered here is very narrow (0–250 keV), no steep change in the combinatorial background contribution is expected; thus, it can be parametrized using a first-order polynomial $f(E_{\text{c.m.}}) = a_0 + a_1 E_{\text{c.m.}}$ [62]. The a_0 and a_1 constants that were used to parametrize the background shown in Fig. 12 were allowed to assume their minimum, maximum, and best-fit values to determine the lower, upper, and best estimates of the N_1 and N_2 parameters describing the resonance top values. The corresponding errors are marked with the "back." subscript in Table III. Regarding the uncertainty owing to the correlation between the N_1 and N_2 values in the fit (marked by the subscript "corr." in Table III), the maximum (minimum) value of N_1 was evaluated fixing the minimum (maximum) value of N_2 allowed by the fit. The two parameters N_1 and N_2 obtained in LNS and NSL experiments are reported in Table III with their errors, where the subscripts 1 and 2 refer to the 65- and 183-keV resonances, respectively. From the comparison between these two sets of TH data, a good agreement is shown within the experimental errors.

The knowledge of the obtained N_i peak values bears a fundamental physical meaning in case of narrow resonances. In fact, they are easily connected to the resonance strengths $(\omega\gamma)_i$ corresponding to the ^{18}F levels [63], which are the key parameters for evaluating the reaction rate for astrophysical applications. Following Ref. [63], the resonance strength for the ith state can be defined as

$$(\omega\gamma)_i = \frac{2J_{^{18}\text{F}_i} + 1}{(2J_{^{17}\text{O}} + 1)(2J_p + 1)} \frac{\Gamma_{(p^{17}\text{O})_i}(E_{R_i})\Gamma_{(\alpha^{14}\text{N})_i}(E_{R_i})}{\Gamma_i(E_{R_i})}, \quad (14)$$

where $J_{^{17}\text{O}}$, J_p, and $J_{^{18}\text{F}_i}$ are the spins of the ^{17}O nucleus, the proton, and the intermediate ^{18}F resonance, respectively, through which the reaction proceeds and $\Gamma_{(p^{17}\text{O})_i}(E_{R_i})$ represents the partial widths for the $p + {}^{17}\text{O} \rightarrow {}^{18}\text{F}_i$ channel leading to the population of the ith excited state in ^{18}F. From Eqs. (13) and (14) the connection between the N_i parameters, experimentally determined by means of the THM, and the resonance strength $(\omega\gamma)_i$ of the ith resonance can be determined [31,47],

$$(\omega\gamma)_i = \frac{1}{2\pi}\omega_i N_i \frac{\Gamma_{(p^{17}\text{O})_i}(E_{R_i})}{\sigma_{R_i}(\theta)}, \quad (15)$$

where $\omega_i = (2J_{^{18}\text{F}_i} + 1)/[(2J_{^{17}\text{O}} + 1)(2J_p + 1)]$ $(i = 1,2)$ is the statistical factor. This result represents the main advantage of using THM in the investigation of low-energy resonances,

i.e., the possibility of connecting the ith resonance strength $(\omega\gamma)_i$ with the experimentally measured quantity N_i. In addition, such procedure overcomes the need to introduce the spectroscopic factor in the evaluation of the resonance partial width [47].

Indeed, no spectroscopic factor enters Eq. (15) because it cancels out in the $\Gamma_{(p^{17}\mathrm{O})_i}/\sigma_{R_i}(\theta)$ ratio. Because the entrance channel partial width of the ith resonance, intervening in the $^{17}\mathrm{O}(p,\alpha)\,^{14}\mathrm{N}$ reaction, is given by

$$\Gamma_{(p^{17}\mathrm{O})_i} = \frac{3\hbar^2}{\mu_{p^{17}\mathrm{O}} r^2} P_{l_{p^{17}\mathrm{O}}} \theta^2_{p^{17}\mathrm{O}}, \tag{16}$$

it contains the S_i spectroscopic factor appearing in the $\theta^2_{p^{17}\mathrm{O}}$ dimensionless reduced width

$$\theta^2_{p^{17}\mathrm{O}} = \frac{1}{3} S_i r^3 |R(r)|^2, \tag{17}$$

where r is the nuclear interaction radius and $R(r)$ is the radial form factor [64].

However, the transfer reaction cross section for the process $^{17}\mathrm{O}+d \rightarrow {}^{18}\mathrm{F}_i$ is also proportional to the spectroscopic factor S_i, being the corresponding PWIA reaction amplitude [48]

$$M_i \approx \varphi_d(p_{pn})\, W^{^{18}\mathrm{F}_i}_{p^{17}\mathrm{O}}(\vec{p}_{p^{17}\mathrm{O}}). \tag{18}$$

In this equation $\varphi_d(p_{pn})$ is the Fourier transform of the s-wave radial wave function for the p-n bound state, p_{pn} is the p-n relative momentum (equal to the neutron momentum p_s in the system where deuteron is at rest), while

$$W^{^{18}\mathrm{F}_i}_{p^{17}\mathrm{O}}(\vec{p}_{p^{17}\mathrm{O}}) = \left\langle I^{^{18}\mathrm{F}_i}_{p^{17}\mathrm{O}} | V_{p^{17}\mathrm{O}} | \vec{p}_{p^{17}\mathrm{O}} \right\rangle \tag{19}$$

is the form factor for the $^{17}\mathrm{O}+p \rightarrow {}^{18}\mathrm{F}_i$ process, leading to the ith excited state in $^{18}\mathrm{F}$. Here $I^{^{18}\mathrm{F}_i}_{p^{17}\mathrm{O}}$ is the $^{17}\mathrm{O}+\mathrm{p} \rightarrow {}^{18}\mathrm{F}_i$ overlap function, $\vec{p}_{p^{17}\mathrm{O}}$ is the relative momentum, and $V_{p^{17}\mathrm{O}}$ is the interaction potential of the $^{17}\mathrm{O}$-p system. In the calculation, $I^{^{18}\mathrm{F}_i}_{p^{17}\mathrm{O}}$ is approximated by $S_i^{1/2}\,\varphi_{(^{17}\mathrm{O}-p)_i}$, where $\varphi_{(^{17}\mathrm{O}-p)_i}$ is the single-particle bound-state wave function for the $^{18}\mathrm{F}_i$ resonance state and S_i the spectroscopic factor for the $^{17}\mathrm{O}+p \rightarrow {}^{18}\mathrm{F}_i$ configuration. Because the spectroscopic factor S_i enters in the calculation of $(W^{^{18}\mathrm{F}_i}_{p^{17}\mathrm{O}})^2$ by Eq. (19) [i.e., in the determination of $\sigma_{R_i}(\theta)$], its effects will be canceled out in the THM $(\omega\gamma)_i$ determination.

In this work we did not measure the absolute value of the cross section; thus, the absolute strength of the resonance at 65 keV was obtained from the ratio between the N_1 and N_2 peak values through the relation [31,47]

$$(\omega\gamma)_1 = \frac{\omega_1}{\omega_2} \frac{\Gamma_{(p^{17}\mathrm{O})_1}}{\sigma_{R_1}(\theta)} \frac{\sigma_{R_2}(\theta)}{\Gamma_{(p^{17}\mathrm{O})_2}} \frac{N_1}{N_2} (\omega\gamma)_2. \tag{20}$$

In particular, for both LNS and NSL experiments, the normalization has been performed by scaling the strength of the 65-keV resonance, $(\omega\gamma)_1$, to the 183-keV one, $(\omega\gamma)_2$, which is well known from the literature. In more detail, the adopted value for the strength of the 183-keV resonance is $(\omega\gamma)_2 = (1.67 \pm 0.07) \times 10^{-3}$ eV, obtained by the weighted average of the four strength values reported in literature [11,21,25,26].

TABLE IV. Summary of the 65-keV resonance strengths obtained in the LNS experiment and in the NSL experiment. The adopted value is the weighted average between the two values obtained in the present work.

Experiment	$(\omega\gamma)_1^{\mathrm{THM}}$ (eV)
LNS	$(3.72 \pm 0.78) \times 10^{-9}$
NSL	$(3.16 \pm 0.68) \times 10^{-9}$
Adopted	$(3.42 \pm 0.60) \times 10^{-9}$

By using this value in Eq. (20), one gets the strength of the resonance at 65 keV for the LNS, $(\omega\gamma)_1^{\mathrm{THM}} = (3.72 \pm 0.78) \times 10^{-9}$ eV, and for the NSL experiment, namely $(\omega\gamma)_1^{\mathrm{THM}} = (3.16 \pm 0.68) \times 10^{-9}$ eV. These values are reported in Table IV. The total error ($\sim$21% for the LNS experiment and $\sim$22% for the NSL experiment) on the two $(\omega\gamma)_1^{\mathrm{THM}}$ values is the sum in quadrature of the independent uncertainties (20.6% for LNS experiment and 21.4% for NSL experiment) owing to the statistical error, the combinatorial background subtraction, and peak-value correlation (see Table III) and of the common uncertainty owing to the normalization procedure (4.2% for both LNS and NSL experiments). Considering the upper and lower limits, the resulting weighted average $(\overline{\omega\gamma})_1^{\mathrm{THM}} = (3.42 \pm 0.60) \times 10^{-9}$ is in good agreement with the strength given by NACRE, $(\omega\gamma)_N = (5.5^{+1.8}_{-1.5}) \times 10^{-9}$ eV [6], and with the direct value, $(\omega\gamma)_D = (4.7 \pm 0.8) \times 10^{-9}$ eV, calculated by using the same Γ_p and Γ_α reported in Refs. [11,21], namely $\Gamma_\alpha = 130$ eV [23] and $\Gamma_p = 19 \pm 3$ neV [18,20]. The $(\overline{\omega\gamma})_1^{\mathrm{THM}}$ value is, at the end, in agreement with the value $(3.66^{+0.76}_{-0.64}) \times 10^{-9}$ eV measured in the previous THM analysis, which has been instead deduced considering the only three 183-keV resonance strength values reported in the literature [11,25,26].

The procedure adopted here, following from Eq. (20), has the main advantage of using, in both cases, the very well studied 183-keV resonant level for normalization purposes, being its resonance strength known within $\sim$4%. Therefore, this approach can be profitably used whenever high-accuracy direct data are available, which is the usual condition in nuclear astrophysics studies with stable beams. Moreover, Eq. (20) allows one to by pass standard normalization procedures, requiring measurement of collected charge, target thickness determination, and dead-time evaluation, which might introduce large systematic errors in the determination of low-energy resonance strengths via direct measurements. A further advantage of Eq. (20) is the presence of the quantity $\frac{\Gamma_{(p^{17}\mathrm{O})_1}}{\sigma_{R_1}(\theta)} \times \frac{\sigma_{R_2}(\theta)}{\Gamma_{(p^{17}\mathrm{O})_2}}$. These two terms are calculated for two close resonances; thus systematic effects owing to the adopted model and parameters (wave functions, potential wells, cutoff radii) cancel out to a large degree.

Additionally, the use of the simple PWIA instead of the more advanced DWBA approach is justified, because the THM relies on the ratio between the two transfer reaction cross sections used to populate the ith $^{18}\mathrm{F}$ level. Absolute values are obtained here through scaling of the THM strengths to the one of the 183-keV resonance; thus, the PWIA assumption turns out to be fully justified as no absolute values are required.

TABLE V. Summary of parameters of the 24 levels in ^{18}F for the ^{17}O$(p,\alpha)\,^{14}$N reaction rates adopted in Ref. [21]. For the subthreshold resonances ($E_R < 0$) the dimensionless reduced width $\theta^2_{p^{17}\mathrm{O}}$ is listed instead of the entrance channel partial width.

E_R (keV)	J^π	Γ_p (eV)	Γ_α (eV)	Γ_γ (eV)
-3.12 ± 0.57	1^+	0.054 ± 0.018	42.8 ± 1.6	0.485 ± 0.051
-1.64 ± 0.57	1^-	8.2×10^{-3}	32.0 ± 2.1	0.894 ± 0.074
65.1 ± 0.5	1^-	$(19.0 \pm 3.2) \times 10^{-9}$	130 ± 5	0.44 ± 0.02
183.35 ± 0.25	2^-	$(4.00 \pm 0.24) \times 10^{-3}$	13.3 ± 5.5	$(9.6 \pm 3.6) \times 10^{-3}$
489.9 ± 1.2	4^-	138 ± 26	106 ± 17	0.1 ± 0.001
501.5 ± 3.0	1^+	0.20 ± 0.02	33.6 ± 3.3	0.1 ± 0.001
556.7 ± 1.0	3^+	$(14.0 \pm 0.5) \times 10^3$	5.0 ± 0.6	0.1 ± 0.001
633.9 ± 0.9	3^-	58.2 ± 7.0	133 ± 24	0.1 ± 0.001
635.5 ± 3.0	3^-	40.8 ± 3.7	137 ± 35	0.1 ± 0.001
655.5 ± 2.5	1^+	27 ± 3	575 ± 120	0.1 ± 0.001
676.7 ± 1.0	2^+	$(10.0 \pm 0.5) \times 10^3$	27 ± 3	0.1 ± 0.001
704.0 ± 0.9	3^+	(525 ± 117)	426 ± 82	0.1 ± 0.001
779.0 ± 1.8	2^+	(109 ± 11)	286 ± 87	0.1 ± 0.001
878.4 ± 1.6	3^+	(277 ± 91)	123 ± 25	0.1 ± 0.001
960.5 ± 1.6	5^+	(1.2 ± 0.1)	560 ± 132	0.1 ± 0.001
1026.5 ± 10.0	1	$(29.20 \pm 3.15) \times 10^2$	$(77.09 \pm 2.00) \times 10^3$	0.1 ± 0.001
1037.2 ± 0.9	2^-	368 ± 61	231 ± 40	0.1 ± 0.001
1170.5 ± 1.5	4^+	$(9 \pm 1) \times 10^3$	150 ± 24	0.1 ± 0.001
1202.5 ± 5.0	2^-	$(16.57 \pm 1.60) \times 10^3$	$(71.5 \pm 2.0) \times 10^3$	0.1 ± 0.001
1204.5 ± 10.0	2	$(2.75 \pm 0.45) \times 10^3$	210 ± 67	0.1 ± 0.001
1250.5 ± 10.0	3	$(5 \pm 1) \times 10^3$	30 ± 7	0.1 ± 0.001
1594.5 ± 2.1	4^-	$(29.4 \pm 1.0) \times 10^3$	500 ± 58	0.1 ± 0.001
1640.5 ± 2.1	1	$(5 \pm 1) \times 10^3$	$(55 \pm 5) \times 10^3$	0.1 ± 0.001
1684.5 ± 2.1	1	$(158.20 \pm 14.26) \times 10^2$	$(441.80 \pm 150.00) \times 10^2$	0.1 ± 0.001

B. Reaction rate evaluation

In the calculation of the ^{17}O$(p,\alpha)\,^{14}$N reaction rate, we followed the method based on Monte Carlo technique adopted in Ref. [21]. This procedure results in a median rate together with a low and a high rate at each temperature, corresponding to the 0.16 and 0.84 quantiles of the cumulative reaction-rate distribution [21].

In the narrow resonance approximation, which is fulfilled for the resonance under investigation, the reaction rate has been deduced through the relations [6]

$$N_A\langle\sigma v\rangle_R = 1.5394 \times 10^{11}(AT_9)^{-3/2} \times \sum_i (\omega\gamma)_i \exp(-11.605 E_{R_i}/T_9), \quad (21)$$

where the incoherent sum is over all narrow resonances i. In this expression, A is the reduced mass, $N_A\langle\sigma v\rangle_R$ is expressed in cm^3 mol^{-1} s^{-1}, and E_{R_i} and $\omega\gamma$ are expressed in MeV.

In our calculation we have associated the measured 65-keV resonance strength, $(\overline{\omega\gamma})_1^{\mathrm{THM}}$ (see Table IV), and its corresponding uncertainty with the expectation value and the square root of the variance of a lognormal distribution, respectively. The excitation energy, $E_R = 65.1 \pm 0.5$ keV [11], was described by a Gaussian probability density function. The interference effect between the resonances at $E_R = 65$ keV and $E_R = -1.64$ keV was also investigated, as well as the interference effect between the resonances at $E_R = 183$ keV and $E_R = 1202$ keV. The effect was found to be smaller than 1% in the temperature range between 0.02 and 0.07 GK, where the ^{17}O$(p,\alpha)\,^{14}$N reaction rate is dominated by the 65-keV resonance. In the reaction-rate calculation, the contributions of the high-energy resonances ($E_R \geqslant 183$ keV), as well as the subthreshold resonance contributions, have been maintained as in Ref. [21] (see Table V for the adopted resonance parameters). Thus, the total reaction rate $N_A\langle\sigma v\rangle_{\mathrm{tot}}^{\mathrm{THM}}$ can be calculated using the relation

$$N_A\langle\sigma v\rangle_{\mathrm{tot}}^{\mathrm{THM}} = N_A\langle\sigma v\rangle_{\mathrm{tot}}^{\mathrm{Iliadis}} - N_A\langle\sigma v\rangle_{65}^{\mathrm{Iliadis}} + N_A\langle\sigma v\rangle_{65}^{\mathrm{THM}}, \quad (22)$$

where $N_A\langle\sigma v\rangle_{\mathrm{tot}}^{\mathrm{Iliadis}}$ is the total reaction rate calculated in Ref. [21].

Figure 13 shows the ratio (red middle line) between the reaction rate R extracted here by Eq. (22) and the reaction rate R_{Iliadis} [21] including the levels listed in Table V. The other red lines in Fig. 13 mark the positions of the high and low rates as deduced in this work. The blue area represents the range of variation for the reaction rate of Iliadis *et al.* [21]. A significant variation (~30%) can be seen in the range $T_9 =$ 0.02–0.07, while no significant differences are present for higher temperatures. The definition of the resonance strength [Eq. (14)] enables us to provide a new value for the strength of the $E_R = 65$ keV resonance in the ^{17}O$(p,\gamma)\,^{18}$F channel as well. Because the $\omega\gamma$ parameter of the $E_R = 65$ keV resonance in the ^{17}O$(p,\alpha)\,^{14}$N reaction is proportional to the proton partial width Γ_p, the exit channel partial width essentially coinciding with the total width through the statistical factor, and because the strength of the 65-keV resonance in the

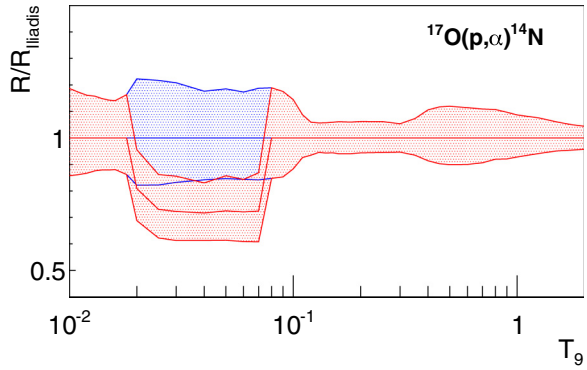

FIG. 13. (Color online) Comparison of the THM reaction rate of the ^{17}O(p,α) ^{14}N reaction with the direct one [21]. The blue area is used to display the range on uncertainty characterizing direct data [21]. The red area, instead, marks the reaction-rate interval allowed by the experimental uncertainties on the 65-keV resonance strength only, as listed in Table III.

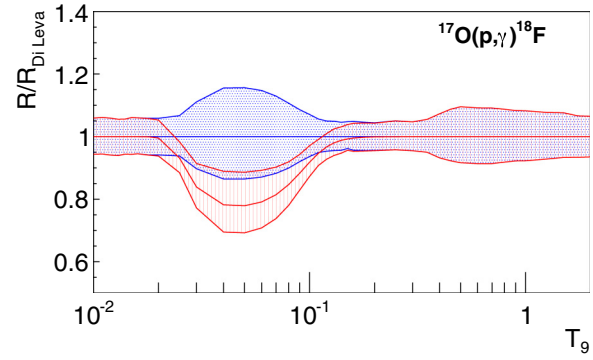

FIG. 14. (Color online) Comparison of the THM reaction rate of the ^{17}O(p,γ) ^{18}F reaction with the direct one [28]. The blue area is used to display the range on uncertainty characterizing direct data [28]. The red area, instead, marks the reaction-rate interval allowed by the experimental uncertainties on the 65-keV resonance strength only, as listed in Table III.

^{17}O(p,γ) ^{18}F channel is proportional to Γ_p as well, by using the formula

$$(\omega\gamma)^{\rm THM}_{p\gamma} = (\omega\gamma)^{\rm THM}_{p\alpha}\frac{\Gamma_\gamma}{\Gamma_\alpha}, \qquad (23)$$

the 65-keV resonance strength in the (p,γ) channel can be evaluated. The Γ_γ and Γ_α values used in Eq. (23) are those listed in Table V.

This results in a THM-scaled resonance strength of the 65-keV resonance of $(\omega\gamma)^{\rm THM}_{p\gamma} = (1.18 \pm 0.21) \times 10^{-11}$ eV. This is lower than the value of $(1.64 \pm 0.28) \times 10^{-11}$ eV given in the literature and in the most recent reviews [9,11,19,21,65]. This 39% difference between the THM-scaled resonance strength and the value in the literature might determine significant consequences on astrophysics motivating an evaluation of its reaction rate. To compare the ^{17}O(p,γ) ^{18}F reaction rate R extracted here, including the THM-scaled resonance strength, with the most recent reaction-rate evaluation $R_{\rm DiLeva}$ of Di Leva *et al.* [28], the recommended values and the upper and lower limits were deduced as evaluated in the NACRE compilation [6]. Figure 14 shows the ratio (red middle line) between the reaction rate R extracted here, including THM-scaled resonance strength for the ^{17}O(p,γ) ^{18}F reaction, and the reaction rate evaluation $R_{\rm DiLeva}$ of Di Leva *et al.* [28]. The recommended upper and lower limits are marked by red lines. The upper and lower limits account for the uncertainty on the THM-scaled resonance strength. In the same way, a blue area is used to show the Di Leva *et al.* [28] reaction rate. A clearly 20% reduction of the reaction rate between $T_9 \sim 0.03$ and $\sim$0.09 can be observed owing to the reduction of the proton partial width Γ_p as a consequence of the THM measurement of the 65-keV resonance strength.

As discussed in Ref. [31], a possible explanation for the discrepancies between direct and THM results in both (p,α) and (p,γ) channels could be attributable to the electron screening effect that was not taken into account in the direct measurements. The screening effect leads to an enhancement of the bare nucleus cross section $\sigma_b(E)$ by a factor $f_{\rm enh}$ defined in Eq. (4). Because the THM data are not affected by the electron screening, the ratio of the direct strength $(\omega\gamma)_{\rm DIR.}$ [11,21] to the THM one provides an estimate of $f_{\rm enh}$ as

$$f_{\rm enh} = \frac{(\omega\gamma)_{\rm DIR.}}{(\omega\gamma)_{\rm THM}} = e^{\pi\eta(E_{R_i})\frac{U_e}{E_{R_i}}}, \qquad (24)$$

where $\eta(E_{R_i})$ is the Sommerfeld parameter evaluated at the resonance energy $E_{R_i} = 65$ keV. Eq. (24) leads to

$$f_{\rm enh} = 1.37 \pm 0.33, \qquad (25)$$

where the error has been evaluated trough the standard error propagation procedure. Our result is in agreement with the theoretical value $f_{\rm enh} = 1.148$ given in Ref. [32]. To cross-check our explanation of the lower TH $\omega\gamma$ value, the experimental electron screening potential U_e was determined, setting $f_{\rm lab} = 1.37$ in Eq. (4). Because of the large uncertainties affecting the enhancement factor $f_{\rm enh}$, only an estimate of the electron screening potential is viable, providing $U_e = 1356 \pm 1037$ eV. This was compared with the theoretical upper limit provided by the adiabatic approximation, $U_e^{\rm ad} = 594$ eV [32–34]. Though our estimate is much larger than $U_e^{\rm ad}$, it is a reasonable evaluation supporting the TH approach, because the experimental U_e value was found to be much larger than the adiabatic limit in many reactions studied so far ([33] and references therein). This is a well-known source of the systematic uncertainty affecting direct low-energy cross-section measurements and requiring extrapolation from higher energies to extract reliable information on the cross section at astrophysical energies.

VII. CONCLUSION

In this work, we report on two independent applications of the THM to the QF ^{2}H(^{17}O,α ^{14}N)n reaction for extracting the ^{17}O(p,α) ^{14}N reaction rate, by using the approach for resonance case discussed in Ref. [47].

The main results of the LNS experiment were already published in Ref. [31], where the value of $(\omega\gamma)^{\rm THM}_1 = (3.66^{+0.76}_{-0.64}) \times 10^{-9}$ eV was evaluated for the 65-keV resonance strength. This adopted value was obtained by means of a

normalization procedure to the 183-keV resonance strength values as given in Refs. [11,25,26].

In the present paper the detailed data analysis of the LNS and at NSL experiments are extensively discussed. It provided

$(\omega\gamma)_1^{\rm THM} = (3.72 \pm 0.78) \times 10^{-9}$ eV for the LNS experiment and $(\omega\gamma)_1^{\rm THM} = (3.16 \pm 0.68) \times 10^{-9}$ eV for the NSL experiment for the strength of the ^{18}F resonance at 65 keV. These values were obtained by introducing the 183-keV resonance strength reported in Ref. [21] in the normalization procedure discussed in Ref. [31]. The weighted average of the these two values $(\overline{\omega\gamma})_1^{\rm THM} = (3.42 \pm 0.60) \times 10^{-9}$ eV is in agreement with the one reported in Ref. [31] and it was used as an input parameter to perform the ^{17}O$(p,\alpha)\,^{14}$N reaction-rate calculation. A significant difference of $\sim$30% with respect the literature data [21] was found in the temperature range relevant for red giant, AGB and massive stars. In addition, by using the definition of the resonance strength, the $E_R = 65$ keV strength for the (p,γ) channel was calculated and used in the ^{17}O$(p,\gamma)\,^{18}$F reaction-rate evaluation. Its comparison with the direct data [28] shows a difference of $\sim$20%.

Thanks to this approach, suited to extract the resonance strength for narrow resonances, the obtained results do not suffer form distortion and eventual dependence on the theoretical analysis and their discrepancy between direct and THM data can be explained by taking into account the electron screening effect. Although the large uncertainties do not allow to make any definitive conclusions, the adopted U_e value extracted here deviates by a factor $\sim$2.3 from the adiabatic model, corroborating once again the discrepancy between theoretical expectations and experimental measurements, largely discussed in the literature.

As a next step, the astrophysical implications of this work have to be evaluated and they will be the subject of a forthcoming dedicated paper.

ACKNOWLEDGMENTS

This work has been partially supported by the Italian Ministry of University MIUR under Grants No. RFBR082838 (FIRB2008) and "LNS-Astrofisica Nucleare (fondi premiali)." It has been partially supported also by Grants No. LC 07050 of the Czech MŠMT, No. M10480902 of the Czech Academy of Science, and No. LH1101 of the AMVIS project. A.M.M. acknowledges that this material is based upon his work supported by the U.S. Department of Energy, Office of Science, Office of Nuclear Science, under Awards Nos. DE-FG02-93ER40773 and DE-SC0004958. A.M.M. also acknowledges the support by the DOE-NNSA under Award No. DE-FG52-09NA29467 and by the U.S. National Science Foundation under Award No. PHY-1415656.

APPENDIX

In the PWIA, the cross section of the three-body reaction $a + A \longrightarrow s + b + B$, can be written as [66]

$$\frac{d^3\sigma}{d\Omega_b d\Omega_B dE_b} \propto KF \cdot |\phi(\vec{p}_s)|^2 \cdot \left(\frac{d\sigma}{d\Omega}\right)^{\rm HOES}, \qquad \text{(A1)}$$

where

(i) KF is a kinematical factor containing the final-state phase-space factor and it is a function of the masses, momenta and emission angles of the two detected particles b and B;

(ii) $\phi(\vec{p}_s)$ is the Fourier transform of the radial wave function $\chi(\vec{r}_{xs})$ of the x-s intercluster motion;

(iii) $(\frac{d\sigma}{d\Omega})^{\rm HOES}$ is the half-off-energy-shell (HOES) differential cross section for the binary $A(x,b)B$ reaction at the center-of-mass energy $E_{\rm c.m.}$, given in postcollision prescription by the relation [67]

$$E_{\rm c.m.} = E_{bB} - Q, \qquad \text{(A2)}$$

where Q is the Q value for the binary reaction and E_{bB} is the relative energy between the two detected particles, b and B.

The HOES behavior of the $A(x,b)B$ differential cross section in Eq. (A1) is attributable to the deviation from the mass shell equation for the A-x system, for which the corresponding relative energy E_{Ax} is defined as

$$E_{Ax} = \frac{p_{Ax}^2}{2\mu_{Ax}} - \frac{p_{sx}^2}{2\mu_{sx}} - \epsilon_{sx}, \qquad \text{(A3)}$$

p_{ij} and μ_{ij} being the relative momentum and the reduced mass for the i-j system (either A-x or s-x), respectively, and ϵ_{sx} the binding energy for the s-x system inside a. Equation (A3) can be further reduced to

$$E_{Ax} = \frac{p_{Ax}^2}{2\mu_{Ax}} - \epsilon_{sx}, \qquad \text{(A4)}$$

if one assumes an s-wave x-s relative motion (like the p-n motion inside deuteron or the p-d motion inside ^{3}He) and a QF kinematics, for which $p_{xs} = 0$. Thus, in the entry channel $E_{Ax} \neq \frac{p_{Ax}^2}{2\mu_{Ax}}$. On the contrary, the particles b and B, in the exit channel, are on shell, being their relative kinetic energy related to the corresponding momenta through the mass-shell equation.

As already discussed, for resonant cases, the TH double differential cross section can be written as [46,48–50]

$$\frac{d^2\sigma^{\rm TH}}{d\Omega_{\mathbf{k}_{sF}} dE_{bB}} = \frac{1}{2\pi} \frac{\Gamma_{bB}(E_{bB})}{\left(E_{bB} - E_{R_{bB}}\right)^2 + \frac{1}{4}\Gamma^2(E_{bB})} \times \frac{d\sigma_{(a+A\to s+F)}}{d\Omega_{\mathbf{k}_{sF}}}, \qquad \text{(A5)}$$

where the differential $\frac{d\sigma_{(a+A\to s+F)}}{d\Omega_{\mathbf{k}_{sF}}}$ cross section has the form [50]

$$\frac{d\sigma_{(a+A\to s+F)}}{d\Omega_{\hat{\mathbf{k}}_{sF}}} = \frac{\mu_{sF}\,\mu_{aA}}{4\pi^2} \frac{k_{sF}}{k_{aA}} \frac{1}{\hat{J}_A\,\hat{J}_a} \times \sum_{M_F\,M_s\,M_A\,M_a} \left|M_{M_F\,M_s;M_A\,M_a}(\mathbf{k}_{sF},\mathbf{k}_{aA})\right|^2, \qquad \text{(A6)}$$

J_i and M_i being the spin of particle i and its projection, respectively. In PWIA, the transfer reaction amplitude M can be factorized as

$$M_i \approx \phi(p_{xs})\, W_{xA}^{{\rm F}_i}(\mathbf{p}_{xA}), \qquad \text{(A7)}$$

where $\phi(p_{xs})$ is the Fourier transform of the radial x-s bound-state wave function, p_{xs} is the x-s relative momentum, while

$$W_{xA}^{\mathrm{F}_i}(\mathbf{p}_{xA}) = \left\langle I_{xA}^{\mathrm{F}_i} | V_{xA} | \mathbf{p}_{xA} \right\rangle \tag{A8}$$

is the form factor for the $A + x \rightarrow \mathrm{F}_i$ process, leading to the feeding of the ith excited state F_i. Therefore, Eq. (A5) represents an extension of Eq. (A1) to the case of resonant reactions and makes it possible to use more-advanced approaches in the place of PWIA, such as DWBA or Continuum Discretized Coupled Channels. Indeed, when PWIA is used to calculate the $\frac{d\sigma_{(a+A\rightarrow s+F)}}{d\Omega_{\mathbf{k}_{sF}}}$ differential cross section, Eq. (A5) takes a form similar to the one of Eq. (A1), because they both contain information about the QF process (through the square modulus of the Fourier transform of the radial wave function for the x-s system) and the population of the F_i resonant state through the binary $A + x$ subreaction.

[1] D. D. Clayton and F. Hoyle, Astrophys. J. **187**, L101 (1974).
[2] D. D. Clayton, Astrophys. J. **244**, L97 (1981).
[3] M. D. Leising and D. D. Clayton, Astrophys. J. **323**, 159 (1987).
[4] R. Diehl, Astron. Rev. **8**, 16 (2013).
[5] M. Hernanz *et al.*, Astrophys. J. **526**, L97 (1999).
[6] C. Angulo *et al.* (NACRE), Nucl. Phys. A **656**, 3 (1999).
[7] K. Nollet *et al.*, Astrophys. J. **582**, 1036 (2003).
[8] G. J. Wasserburg *et al.*, Astrophys. J. Lett. **447**, L37 (1995).
[9] S. Palmerini *et al.*, Astrophys. J. **764**, 128 (2013).
[10] J. José *et al.*, J. Phys. G: Nucl. Part. Phys. **34**, R431 (2007).
[11] A. Chafa *et al.*, Phys. Rev. C **75**, 035810 (2007).
[12] V. Landre *et al.*, Phys. Rev. C **40**, 1972 (1989).
[13] D. Tilley *et al.*, Nucl. Phys. A **595**, 1 (1995).
[14] J. C. Blackmon, A. E. Champagne, M. A. Hofstee, M. S. Smith, R. G. Downing, and G. P. Lamaze, Phys. Rev. Lett. **74**, 2642 (1995).
[15] R. Brown, Phys. Rev. **125**, 347 (1962).
[16] C. Rolfs and W. Rodney, Nucl. Phys. A **250**, 295 (1975).
[17] M. Berheide *et al.*, Z. Phys. A **343**, 483 (1992).
[18] M. Hannam and W. Thompson, Nucl. Instrum. Methods A **431**, 239 (1999).
[19] C. Fox *et al.*, Phys. Rev. Lett. **93**, 081102 (2004).
[20] C. Fox *et al.*, Phys. Rev. C **71**, 055801 (2005).
[21] C. Iliadis *et al.*, Nucl. Phys. A **841**, 251 (2010).
[22] I. Berka *et al.*, Nucl. Phys. A **288**, 317 (1977).
[23] H. Mak *et al.*, Nucl. Phys. A **343**, 79 (1980).
[24] W. Kieser *et al.*, Nucl. Phys. A **331**, 155 (1979).
[25] J. R. Newton, C. Iliadis, A. E. Champagne, R. Longland, and C. Ugalde, Phys. Rev. C **75**, 055808 (2007).
[26] B. Moazen *et al.*, Phys. Rev C **75**, 065801 (2007).
[27] D. Scott *et al.*, Phys. Rev. Lett. **109**, 202501 (2012).
[28] A. Di Leva *et al.*, Phys. Rev. C **89**, 015803 (2014).
[29] Ajzenberg-Selove, Nucl. Phys. A **475**, 1 (1987).
[30] C. Rolfs *et al.*, Nucl. Phys. A **199**, 306 (1973).
[31] M. L. Sergi *et al.*, Phys. Rev. C. **82**, 032801(R) (2010).
[32] H. Assenbaum, K. Langanke, and C. Rolfs, Z. Phys. **327**, 461 (1987).
[33] F. Strieder *et al.*, Naturwissenschaften **88**, 461 (2001).
[34] G. Fiorentini *et al.*, Z. Phys. A **350**, 289 (1995).
[35] G. Baur *et al.*, Nucl. Phys. A **458**, 188 (1986).
[36] S. Cherubini *et al.*, Astrophys. J. **457**, 855 (1996).
[37] C. Spitaleri *et al.*, Phys. Rev. C **60**, 055802 (1999).
[38] C. Spitaleri *et al.*, Phys. At. Nuclei **74**, 1763 (2011).
[39] M. La Cognata *et al.*, Astron. Phys. J. Lett. **739**, L54 (2011).
[40] L. Lamia *et al.*, Il Nuovo Cimento della Società Italiana di Fisica C **31**, 423 (2008).
[41] L. Lamia *et al.*, The Astrophys. Journ. **768**, 65 (2013).
[42] R. Pizzone *et al.*, Phys. Rev. C **83**, 045801 (2011).
[43] M. L. Sergi, Il Nuovo Cimento della Società Italiana di Fisica **125B**, 457 (2010).
[44] A. Tumino *et al.*, Phys. Rev. Lett. **98**, 252502 (2007).
[45] R. Tribble *et al.*, Rep. Prog. Phys. **77**, 106901 (2014).
[46] M. La Cognata *et al.*, Phys. Rev. Lett. **101**, 152501 (2008).
[47] M. La Cognata *et al.*, Astrophys. J. **708**, 796 (2010).
[48] E. I. Dolinsky *et al.*, Nucl. Phys. A **202**, 97 (1973).
[49] A. M. Mukhamedzhanov *et al.*, J. Phys. G: Nucl. Part. Phys. **35**, 014016 (2008).
[50] M. La Cognata, V. Z. Goldberg, A. M. Mukhamedzhanov, C. Spitaleri, and R. E. Tribble, Phys. Rev. C. **80**, 012801 (2009).
[51] R. Evans, *The Atomic Nucleus* (McGraw-Hill, New York, 1969).
[52] E. Segré, *Nuclei and Particles* (Benjamin-Cummings, San Francisco, 1977).
[53] G. Ohlsen, Nucl. Instrum. Methods **37**, 240 (1965).
[54] C. Spitaleri *et al.*, Phys. Rev. C **69**, 055806 (2004).
[55] J. Kasagi *et al.*, Nucl. Phys. A **239**, 233 (1975).
[56] M. Zadro, D. Miljanić, C. Spitaleri, G. Calvi, M. Lattuada, and F. Riggi, Phys. Rev. C. **40**, 181 (1989).
[57] R. Pizzone *et al.*, Phys. Rev. C **80**, 025807 (2009).
[58] R. G. Pizzone *et al.*, Phys. Rev. C **71**, 058801 (2005).
[59] I. J. Thompson, Comput. Phys. Rep. **7**, 167 (1987).
[60] C. M. Perey and F. Perey, At. Data Nucl. Data Tables **17**, 1 (1976).
[61] I. S. Shapiro *et al.*, Nucl. Phys. A **61**, 353 (1965).
[62] M. La Cognata *et al.*, Phys. Rev. C **76**, 065804 (2007).
[63] C. Rolfs and W. Rodney, *Cauldrons in the Cosmos* (University of Chicago Press, Chicago, 1988).
[64] A. Champagne and M. Pitt, Nucl. Phys. A **457**, 637 (1986).
[65] E. G. Adelberger *et al.*, Rev. Mod. Phys. **83**, 195 (2011).
[66] C. Spitaleri, in *Interaction of High-Energy Particles with Nuclei, Proceedings of the International School of Physics "Enrico Fermi," Course CLXXVIII*, edited by A. Bracco and E. Nappi (IOS Press, Amsterdam, 2011), p. 210.
[67] J. Grossiodor *et al.*, Phys. Rev. Lett. **32**, 177 (1974).